

AD-A201 131

DTIC FILE COPY

2

ESL-TR-86-49

FACTORS AFFECTING THE ACCURACY OF THE INTEGRATED PARTICLE SIZING SYSTEM

C.L. PROCTOR, B.D. HISAGER, A. TOUATI

THE UNIVERSITY OF FLORIDA COMBUSTION LABORATORY
DEPARTMENT OF MECHANICAL ENGINEERING
GAINESVILLE FL 32611

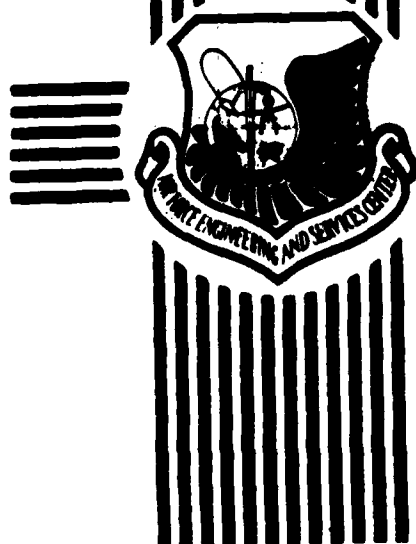
AUGUST 1988

FINAL REPORT

MAY 1983 - OCTOBER 1985

DTIC
ELECTE
OCT 18 1988
S E D

APPROVED FOR PUBLIC RELEASE: DISTRIBUTION UNLIMITED



ENGINEERING & SERVICES LABORATORY
AIR FORCE ENGINEERING & SERVICES CENTER
TYNDALL AIR FORCE BASE, FLORIDA 32403

88 1000 100

NOTICE

PLEASE DO NOT REQUEST COPIES OF THIS REPORT FROM
HQ AFESC/RD (ENGINEERING AND SERVICES LABORATORY).
ADDITIONAL COPIES MAY BE PURCHASED FROM:

NATIONAL TECHNICAL INFORMATION SERVICE
5285 PORT ROYAL ROAD
SPRINGFIELD, VIRGINIA 22161

FEDERAL GOVERNMENT AGENCIES AND THEIR CONTRACTORS
REGISTERED WITH DEFENSE TECHNICAL INFORMATION CENTER
SHOULD DIRECT REQUESTS FOR COPIES OF THIS REPORT TO:

DEFENSE TECHNICAL INFORMATION CENTER
CAMERON STATION
ALEXANDRIA, VIRGINIA 22314

UNCLASSIFIED
SECURITY CLASSIFICATION OF THIS PAGE

REPORT DOCUMENTATION PAGE				Form Approved OMB No. 0704-0188										
1a. REPORT SECURITY CLASSIFICATION UNCLASSIFIED			1b. RESTRICTIVE MARKINGS											
2a. SECURITY CLASSIFICATION AUTHORITY			3. DISTRIBUTION/AVAILABILITY OF REPORT Approved for Public Release Distribution Unlimited											
2b. DECLASSIFICATION/DOWNGRADING SCHEDULE			5. MONITORING ORGANIZATION REPORT NUMBER(S)											
4. PERFORMING ORGANIZATION REPORT NUMBER(S) ESL-TR-86-49			7a. NAME OF MONITORING ORGANIZATION Air Force Engineering and Services Center											
6a. NAME OF PERFORMING ORGANIZATION The University of Florida		6b. OFFICE SYMBOL (If applicable) UFCL	7b. ADDRESS (City, State, and ZIP Code) HQ AFESC/RDVS Tyndall AFB, Florida 32403-6001											
6c. ADDRESS (City, State, and ZIP Code) University of Florida Combustion Laboratory Department of Mechanical Engineering Gainesville, Florida 32611		9. PROCUREMENT INSTRUMENT IDENTIFICATION NUMBER FO8635-C0136, Task 83-03												
8a. NAME OF FUNDING/SPONSORING ORGANIZATION		8b. OFFICE SYMBOL (If applicable)	10. SOURCE OF FUNDING NUMBERS											
8c. ADDRESS (City, State, and ZIP Code)		PROGRAM ELEMENT NO. 62601F	PROJECT NO. 1900	TASK NO. 2059	WORK UNIT ACCESSION NO.									
11. TITLE (Include Security Classification) Factors Affecting the Accuracy of the Integrated Particle Sizing System														
12. PERSONAL AUTHOR(S) Charles L. Proctor, Barbara D. Isager, Abderrahmane Touati														
13a. TYPE OF REPORT Final		13b. TIME COVERED FROM May 83 TO Oct 85		14. DATE OF REPORT (Year, Month, Day) August 1988										
15. PAGE COUNT 74														
16. SUPPLEMENTARY NOTATION Availability of this report is specified on reverse of front cover.														
17. COSATI CODES			18. SUBJECT TERMS (Continue on reverse if necessary and identify by block number)											
<table border="1"><thead><tr><th>FIELD</th><th>GROUP</th><th>SUB-GROUP</th></tr></thead><tbody><tr><td>21</td><td>05</td><td></td></tr><tr><td>21</td><td>02</td><td></td></tr></tbody></table>			FIELD	GROUP	SUB-GROUP	21	05		21	02		Soot Formation Optical Particle Sizing		
FIELD	GROUP	SUB-GROUP												
21	05													
21	02													
19. ABSTRACT (Continue on reverse if necessary and identify by block number) The purpose of this research was to investigate factors affecting instrument accuracy of a nonintrusive optical system known as the Integrated Particle Sizing System (IPSS). Studies of soot formation and growth in laboratory combustors were conducted at the Air Force Engineering and Services Center, Environics Division, using the IPSS. However, the behavior of this instrument and the factors affecting its accuracy were not completely understood, causing the proper operation of the instrument and the interpretation of results to be questioned. This report focused on the theory governing the instrument's design. A list of limitations imposed by theory was derived and measurements were made to verify the relationship between incoming signal, theory, and actual particle size.														
20. DISTRIBUTION/AVAILABILITY OF ABSTRACT <input type="checkbox"/> UNCLASSIFIED/UNLIMITED <input checked="" type="checkbox"/> SAME AS RPT. <input type="checkbox"/> DTIC USERS			21. ABSTRACT SECURITY CLASSIFICATION UNCLASSIFIED											
22a. NAME OF RESPONSIBLE INDIVIDUAL Major Paul E. Kersch			22b. TELEPHONE (Include Area Code) 904 283-4234		22c. OFFICE SYMBOL RDVS									

DD Form 1473, JUN 86

Previous editions are obsolete.

1

SECURITY CLASSIFICATION OF THIS PAGE

UNCLASSIFIED

(The reverse of this page is blank.)

PREFACE

This report was prepared by the University of Florida Combustion Laboratory, Mechanical Engineering Department, Gainesville FL 32611, under Contract Number F08635-C-0136, Task 83-03, for the Air Force Engineering and Services Center, Engineering and Services Laboratory (AFESC/RDVS), Tyndall Air Force Base FL 32403-6001. The project was sponsored by the Air Force Engineering and Services Center. Major Paul E. Kerch was the government project officer. The report summarizes work accomplished between 1 May 1983 and 1 October 1985.

This report has been reviewed by the Public Affairs Office and is releasable to the National Technical Information Services (NTIS). At NTIS, it will be available to the general public, including foreign nations.

This technical report has been reviewed and is approved for publication.

Paul E. Kerch

PAUL E. KERCH, Maj, USAF, BSC
Project Officer

Kenneth T. Denbleyker

KENNETH T. DENBLEYKER, Maj, USAF
Chief, Environmental Sciences Branch

Thomas J. Walker

THOMAS J. WALKER, Lt Col, USAF, BSC
Chief, Environics Division

James R. VanOrman

JAMES R. VAN ORMAN
Deputy Director, Engineering and
Services Center

Accession For	
NTIS GRA&I	<input checked="" type="checkbox"/>
DTIC TAB	<input type="checkbox"/>
Unannounced	<input type="checkbox"/>
Justification	
By	
Distribution/	
Availability Codes	
Dist	Avail and/or Special
A-1	



TABLE OF CONTENTS

Section	Title	Page
I	INTRODUCTION	1
	A. OBJECTIVE.....	1
	B. BACKGROUND.....	1
	C. SCOPE.....	2
II	THE LIMITATIONS OF THE MIE THEORY	3
	A. SCATTERING FUNDAMENTALS.....	3
	B. DISCUSSION OF THE WAVE EQUATION.....	5
	C. THE MIE THEORY.....	8
III	THE INTEGRATED PARTICLE SIZING SYSTEM	26
	A. OPTICAL SYSTEM.....	26
	B. DATA PROCESSING SYSTEM.....	31
	C. DATA MANAGEMENT SYSTEM.....	35
	D. CALIBRATION PARTICLES.....	39
	E. PARTICLE GENERATION SYSTEM.....	39
	F. CALIBRATION AND APPLICATION OF THE IPSS..	39
IV	CONCLUSIONS AND RECOMMENDATIONS	61
	REFERENCES.....	63
APPENDIX		
A	MAXWELL'S EQUATIONS.....	64
	A. GAUSS'S LAW FOR ELECTRIC FIELDS.....	65
	B. GAUSS'S LAW FOR MAGNETIC FIELDS.....	65
	C. FARADAY'S LAW OF INDUCTANCE.....	68
	D. AMPERE'S LAW.....	68
	E. BOUNDARY CONDITIONS.....	70

LIST OF FIGURES

Figure	Title	Page
1	A Physical Representation of the Electromagnetic Radiation Scattered by a Particle.....	10
2	Polar Plots of the Ratio of the Common Logarithm of the Scattered Intensity to Incident Intensity for Particles of Various Sizes and Real Refractive Index.....	22
3	Polar Plots of the Ratio of the Common Logarithm of the Scattered Intensity to Incident Intensity for Particles of Various Sizes and Complex Refractive Index.....	23
4	Plots of Intensity Ratio versus a Wide Range of Particle Sizes for a 40°/20° Angle Pair.....	25
5	Schematic of the IPSS.....	28
6	Percent Transmittance versus Wavelength for IPSS PMT Filters..	30
7	Examples of the Restrictions on Valid and Invalid Data.....	32
8	Plot of Theoretical Intensity Ratio versus Diameter for a 40°/20° Angle Pair and a Real Refractive Index of 1.57.....	33
9	Polar Plots of the Scattered Intensity for a 0.414 μm and a 1.40 μm Particle.....	34
10	Sample Output of the IPSS.....	38
11	TSI Constant Output Atomizer.....	41
12	Diffusion Drier.....	42
13	Measured Linear Mean Diameter versus Nominal Diameter of Latex Spheres.....	44
14	Normalized Graph of Raw Counts versus Size.....	45
15	Comparison of Theoretical Intensity Ratio versus Diameter with the IPSS Bin Center Tables for a 40°/20° Angle Pair and a Real Refractive Index of 1.57.....	47
16	A Closer Examination of the 40°/20° Angle Pair for a Real Refractive Index of 1.57 and the Diametric Range of 0.53 μm to 0.60 μm	48
17	Comparison of Theoretical Intensity Ratio versus Diameter with the IPSS Bin Center Tables for a 50°/20° Angle Pair and a Real Refractive Index of 1.57.....	49

Figure	LIST OF FIGURES (CONTINUED) Title	Page
18	Comparison of Theoretical Intensity Ratio versus Diameter with the IPSS Bin Center Tables for a $60^\circ/20^\circ$ Angle Pair and a Real Refractive Index of 1.57.....	50
19	Plot of Intensity Ratio versus Diameter for an $8^\circ/2.5^\circ$ Angle Pair and a Real Refractive Index of 1.57.....	51
20	Comparison of Theoretical Intensity Ratio versus Diameter with the IPSS Bin Center Tables for a $10^\circ/5^\circ$ Angle Pair and a Real Refractive Index of 1.57.....	52
21	Plot of Intensity Ratio versus Diameter for a $12^\circ/5^\circ$ Angle Pair and a Real Refractive Index of 1.57.....	53
22	Plot of Theoretical Intensity Ratio versus Diameter for an $8^\circ/2.5^\circ$ Angle Pair and a Complex Refractive Index of 1.57-10.56.....	55
23	Comparison of Theoretical Intensity Ratio versus Diameter with the IPSS Bin Center Tables for a $10^\circ/5^\circ$ Angle Pair and a Complex Refractive Index of 1.57-10.56.....	56
24	Plot of Theoretical Intensity Ratio versus Diameter for a $12^\circ/5^\circ$ Angle Pair and a Complex Refractive Index of 1.57-10.56.....	57
25	Comparison of Theoretical Intensity Ratio versus Diameter with the IPSS Bin Center Tables for a $40^\circ/20^\circ$ Angle Pair and a Complex Refractive Index of 1.57-10.56.....	58
26	Comparison of Theoretical Intensity Ratio versus Diameter with the IPSS Bin Center Tables for a $50^\circ/20^\circ$ Angle Pair and a Complex Refractive Index of 1.57-10.56.....	59
27	Comparison of Theoretical Intensity Ratio versus Diameter with the IPSS Bin Center Tables for a $60^\circ/20^\circ$ Angle Pair and a Complex Refractive Index of 1.57-10.56.....	60
A-1	A Physical Representation of Gauss's Law for Electric Fields..	66
A-2	A Physical Representation of Gauss's Law for Magnetic Fields..	67
A-3	A Physical Representation of Faraday's Law of Inductance.....	69
A-4	A Physical Representation of Ampere's Law.....	71
A-5	A Representation of Boundary Conditions Between Two Different Media.....	74

LIST OF SYMBOLS

\vec{E}	electric field
\vec{H}	magnetic field
μ	magnetic permeability($=\mu_0\mu_r$)
ϵ	electric permittivity($=\epsilon_0\epsilon_r$)
σ	conductivity
ρ	volumetric free charge density
\vec{D}	electric flux density
\vec{B}	magnetic flux density
ϵ_0	electric permittivity in a vacuum
ϵ_r	relative permittivity
μ_0	magnetic permeability in a vacuum
μ_r	relative permeability
ω	angular frequency
λ	wavelength
k	wavenumber ($= 2\pi/\lambda$)
k_0	wavenumber in a vacuum
c	speed of light in a vacuum
m	complex refractive index
n	real part of the refractive index
κ	imaginary part of the refractive index

SECTION I

INTRODUCTION

A. OBJECTIVE

Studies of soot formation and growth in laboratory combustors were conducted at the Air Force Engineering and Services Center (AFESC), Environics Division, using a nonintrusive optical system known as the Integrated Particle Sizing System (IPSS). The behavior of this instrument and the factors affecting its accuracy were not completely understood, causing the proper operation of the instrument and the interpretation of previously obtained results to be questioned. The purpose of this research was to investigate factors affecting instrument accuracy. This insight allows the determination of appropriate measures which optimize instrument performance.

B. BACKGROUND

Soot formation studies are of interest because soot is a product of inefficient combustion and a good thermal radiator. Soot deposits on the engine liners of aircraft prevent proper heat transfer and decrease the lifetime of the liner. In addition, soot exhaust emissions make the aircraft vulnerable to infrared detector identification by enemy sensors. The presence of soot can also create a potential health hazard. Small soot particles (less than 1.0 μm in diameter) can enter the lung as they are not easily deposited in nasal passages. It is hoped that soot formation studies can result in production of a model can which can reliably predict this still uninterpreted process of combustion.

Particle size distribution can be measured in several different ways. However, the latest trend is toward obtaining measurements optically through the collection of radiation scattered by a particle. These optical diagnostic techniques possess many advantages over conventional techniques. First, because a focused beam of radiation serves as the probe, the technique provides a means of gathering information in hostile laboratory environments without interfering with the flow field of the combustion process. Second,

the spatial resolution is limited by the optics and the wavelength of the radiation used, and therefore, for visible radiation, can be relatively small (on the order of microns). Third, much information can be gathered in a relatively short period of time (on the order of seconds), thus, leading to good temporal resolution and statistically valid results. The IPSS is a prototype of such an optical diagnostic instrument. During preliminary runs, the IPSS displayed unexpected characteristics which are not explained in the system manual. This behavior prompted questions regarding the instrument's accuracy and initiated this study.

C. SCOPE

In an attempt to answer questions about the IPSS, the theory governing the instrument's design was studied. From this part of the investigation, a list of limitations imposed by theory was derived. The second part of this investigation studied the design of the IPSS. Work was conducted to show that the relationship between the incoming signal and particle size does not agree with that found in theory. This finding was verified. Through this investigation, a better understanding of the IPSS was gained and any modifications to the instrument can be done with full understanding of their impact on the system.

SECTION II

THE LIMITATIONS OF THE MIE THEORY

The Mie Scattering Theory, formulated in 1908, describes the electromagnetic field scattered by a particle of arbitrary size. The expression for the scattered electromagnetic field is obtained through the use of Maxwell's equations and the vector wave equation. In application, an expression for the irradiance (incident energy per unit time per unit area of the receiver) is the desired end result. In finding the Mie expression for the scattered field, several assumptions were made to simplify the problem. The purpose of this section is to point out these assumptions as they appear, to provide an awareness of the limitations imposed by the theory, and to gain a clearer understanding of Mie theory-based instrumentation. Specifically, a foundation is formed which provides the basis for the study of factors affecting instrument accuracy. In addition, the determination of appropriate measures which optimize instrumentation performance without violating theoretical considerations is also allowed.

Geometric optics is no longer valid when the dimensions of a system (lenses, particles, etc.) become comparable to or much smaller than the wavelength of the incident radiation. Therefore, for the particles being considered, the wave nature of light must be examined. For this reason, a brief review of Maxwell's equations and the boundary conditions which lead to the Mie theory are included in Appendix A. Before the development of the Mie theory, some basic concepts of light interaction with matter and its relationship to scattering must be defined.

A. SCATTERING FUNDAMENTALS

As electromagnetic radiation travels through a medium, extinction occurs; that is, the energy along the path of the incident beam is attenuated. The two processes responsible for extinction are scattering and absorption. The latter is not the concern of this paper; however, in simple terms, absorption is a result of the damping of the electromagnetic wave by matter within the medium. This, in turn, causes an increase in the internal energy of the

matter but does not involve reradiation from the material. Scattering, which encompasses reflection, refraction, and diffraction occurs when the incident radiation induces dipole moments in the particle. The dipoles, oscillating with the same frequency as the incident radiation, reradiate the secondary wavelets in all directions. These spherical wavefronts, which now compose the scattered radiation, interfere with each other and form an interference pattern corresponding to the physical geometry and optical properties of the particular scatterer. Examples of such patterns are shown in Figures 2 and 3.

Scattering can be classified as elastic or inelastic, dependent or independent, single or multiple. If the scattered radiation is of the same frequency as the incident radiation, the scattering is said to be elastic; otherwise the scattering is inelastic. Examples of inelastic scattering are Raman and Mandel'stam-Brillouin scattering. When the presence of other particles affect the scattering properties of an individual particle, the scattering is said to be dependent. Independent scattering is experimentally and theoretically easier to analyze because the total irradiance or intensity is simply the sum of the intensities scattered by each particle. For independent scattering to occur, the particles must be "sufficiently far from each other" (Reference 1). One general rule of thumb is that the particles must be a distance of at least three radii from each other (Reference 1). Reference 2 suggests that the clearances between particles should be greater than 0.3 wavelength and that the clearance/diameter ratio should be greater than 0.4. In most cases the criteria for independent scattering is satisfied because particles are usually separated by much larger distances (References 1 and 2). The third classification, multiple scattering, occurs when scattered radiation is incident on another scattering surface. Conversely, single scattering implies that the scattered radiation from one particle propagates directly to the detector without any incidence on other particles that may be present in the particle cloud. Each scattering source scatters the radiation of the original beam only. As suggested by Reference 1, the prevalence of single scattering can easily be determined; if doubling the concentration of scattering particles results in twice the amount of intensity being scattered, then single scattering is dominant.

The following pages show that the scattered electric field, as derived by

Lorenz and later by Mie (References 1, 3, and 4), is a function of the magnitude, wavelength and polarization of the incident field, the refractive indices of both the outside medium and the scattering medium, the size and geometry of the scatterer, the distance from the particle, and the direction of scatter.

B. DISCUSSION OF THE WAVE EQUATION

As previously stated, the vector wave equation is the foundation of the Mie theory and is easily obtained from Maxwell's equations, provided certain assumptions are made along the way. However, the purpose of this discussion is not to derive the wave equation, but to show the assumptions leading to it, making one aware that other possibilities exist for a resulting fundamental equation.

To uncouple the electric field from the magnetic field in Maxwell's equations, and thus achieve an equation in terms of either the electric field or magnetic field only, the curl of Equations (A-3) and (A-4) is taken and Relationships (A-5), (A-6), and (A-7) are substituted accordingly to obtain

$$\nabla \times \nabla \times \vec{E} = \nabla \times \left(- \frac{\partial \mu \vec{H}}{\partial t} \right)$$

(1)

$$\nabla \times \nabla \times \vec{H} = (\nabla \times \sigma \vec{E}) + \left(\nabla \times \frac{\partial \epsilon \vec{E}}{\partial t} \right).$$

If the electromagnetic properties, ϵ , μ , and σ , where ϵ is the electric permittivity, μ is the magnetic permeability, and σ , the conductivity, are assumed isotropic, and if ϵ and μ are assumed time independent, they can be placed outside the curl operations. Furthermore, if the fields are continuous in both time and space, the partial derivative and curl operations can be

interchanged. The result then is

$$\begin{aligned}\nabla \times \nabla \times \vec{E} &= -\mu \frac{\partial}{\partial t} (\nabla \times \vec{H}) \\ \nabla \times \nabla \times \vec{H} &= \sigma (\nabla \times \vec{E}) + \epsilon \frac{\partial}{\partial t} (\nabla \times \vec{E}).\end{aligned}\tag{2}$$

Through another substitution of Equations (A-3) through (A-7) and an assumption that σ is also time-independent, the equations become

$$\begin{aligned}\nabla \times \nabla \times \vec{E} &= -\mu \sigma \frac{\partial \vec{E}}{\partial t} - \mu \epsilon \frac{\partial^2 \vec{E}}{\partial t^2}, \\ \nabla \times \nabla \times \vec{H} &= -\mu \sigma \frac{\partial \vec{H}}{\partial t}.\end{aligned}\tag{3}$$

With the vector identity

$$\nabla \times (\nabla \times \vec{F}) = \nabla(\nabla \cdot \vec{F}) - \nabla^2 \vec{F},\tag{4}$$

the above relationships become

$$\begin{aligned}\nabla^2 \vec{E} - \nabla(\nabla \cdot \frac{\vec{D}}{\epsilon}) &= \mu \sigma \frac{\partial \vec{E}}{\partial t} + \mu \epsilon \frac{\partial^2 \vec{E}}{\partial t^2} \\ \nabla^2 \vec{H} - \nabla(\nabla \cdot \frac{\vec{B}}{\mu}) &= \mu \sigma \frac{\partial \vec{H}}{\partial t} + \mu \epsilon \frac{\partial^2 \vec{H}}{\partial t^2}.\end{aligned}\tag{5}$$

Again using Maxwell's equations, as well as the assumption of isotropic electromagnetic properties, the equations are written as

$$\nabla^2 \vec{E} - \frac{1}{\epsilon} \nabla \rho = \mu \sigma \frac{\partial \vec{E}}{\partial t} + \mu \epsilon \frac{\partial^2 \vec{E}}{\partial t^2}. \quad (6)$$

$$\nabla^2 \vec{H} = \mu \sigma \frac{\partial \vec{H}}{\partial t} + \mu \epsilon \frac{\partial^2 \vec{H}}{\partial t^2}.$$

Assuming that both \vec{E} and \vec{H} can be written as the time harmonic plane waves,

$$\vec{E} = \vec{E}_0 e^{-i(\omega t - kz)} \quad (7)$$

$$\vec{H} = \vec{H}_0 e^{-i(\omega t - kz)},$$

where ω is the angular frequency, k is the wave number, and z is the direction of propagation, the previous equation can be simplified to

$$\nabla^2 \vec{E} - \frac{1}{\epsilon} \nabla \rho = (i\omega\mu\sigma - \omega^2\mu\epsilon)\vec{E} \quad (8)$$

$$\nabla^2 \vec{H} = (i\omega\mu\sigma - \omega^2\mu\epsilon)\vec{H}.$$

Now if the gradient of the volumetric charge density ($\nabla \rho$) is zero, and if the conductivity is zero, or is included in the imaginary part of the refractive index (which is related to the relative permittivity), the previous equations become the wave equations:

$$\nabla^2 \vec{E} + \omega^2 \mu \epsilon \vec{E} = 0$$

(9)

$$\nabla^2 \vec{H} + \omega^2 \mu \epsilon \vec{H} = 0.$$

One final simplification can be made by substituting the relationship $\omega(\mu\epsilon)^{1/2} = k_0 m$, where k_0 is the wave number in a vacuum ($= \omega/(\mu_0 \epsilon_0)^{1/2}$) and m is the refractive index ($= (\epsilon\mu/\epsilon_0 \mu_0)^{1/2}$) of the medium. The wave equation can then be written in a more familiar form:

$$\nabla^2 \vec{E} + k_0^2 m^2 \vec{E} = 0$$

(10)

$$\nabla^2 \vec{H} + k_0^2 m^2 \vec{H} = 0.$$

Thus, the assumptions are as follows:

1. both ϵ , μ , and σ are isotropic, time-independent electromagnetic properties,
2. \vec{E} and \vec{H} can be written as time-harmonic plane waves,
3. the fields are spatially and temporally continuous,
4. either the conductivity, σ , is zero or is included in the measurement of the imaginary part of the refractive index.

The effect of anisotropic electromagnetic properties on the scattered field require that these quantities become tensors. The mathematics then become much more complicated. These effects are not investigated in this report.

C. THE MIE THEORY

The Mie theory is a mathematically complicated expression which requires the use of a computer for its calculation. However, the theory is a general

one, unrestricted by particle size. Other theories exist which are less cumbersome to calculate, but their validities depend on the ratio of particle size to the wavelength of incident radiation. As a result, a range of particle size exists where the Mie theory for particles of arbitrary size cannot be replaced by simpler theories. Reference 5 suggests this range to be $0.6 \lambda_m / \pi n < d < 5 \lambda_m / \pi$, where n is the real part of the refractive index, d is the diameter of the particle, and λ_m , the wavelength of the radiation inside the particle. For diameters smaller than the lower bound, the Rayleigh scattering theory is valid. For diameters larger than the upper bound, a scattering theory for large particles is appropriate. Unfortunately, this theory is also popularly known as the Mie theory, although it is a Mie scattering theory specifically for large particles. The distinction is that the Mie theory discussed in this report is for particles of arbitrary size. Its formal name is actually the Lorenz-Mie theory; however, literature seldom refers to it by this name.

In addition to the four assumptions made in developing the wave equation, more assumptions must be made to arrive at the Mie theory:

1. the scattering is restricted to single, elastic, and independent scattering,
2. the particle is spherical,
3. the particle material is homogeneous,
4. the magnetic permeability of the particle is equal to the magnetic permeability of the outside medium,
5. the relative refractive index--that is, the ratio of the refractive index of the particle to that of the outside medium--must be known,
6. no free surface charge is present on the particle,
7. the incident radiation is plane wave, and
8. the scattered radiation is measured far from the point of scatter so that the longitudinal electric field is negligible.

The schematic of the problem is shown in Figure 1. The azimuthal angle θ is defined as the angle formed by the propagation vectors \vec{k}_i (the direction of propagation of the incident radiation) and \vec{k}_s (the direction of propagation of the scattered radiation). The plane containing this angle is called the plane of scatter. Once this plane is defined, the incident

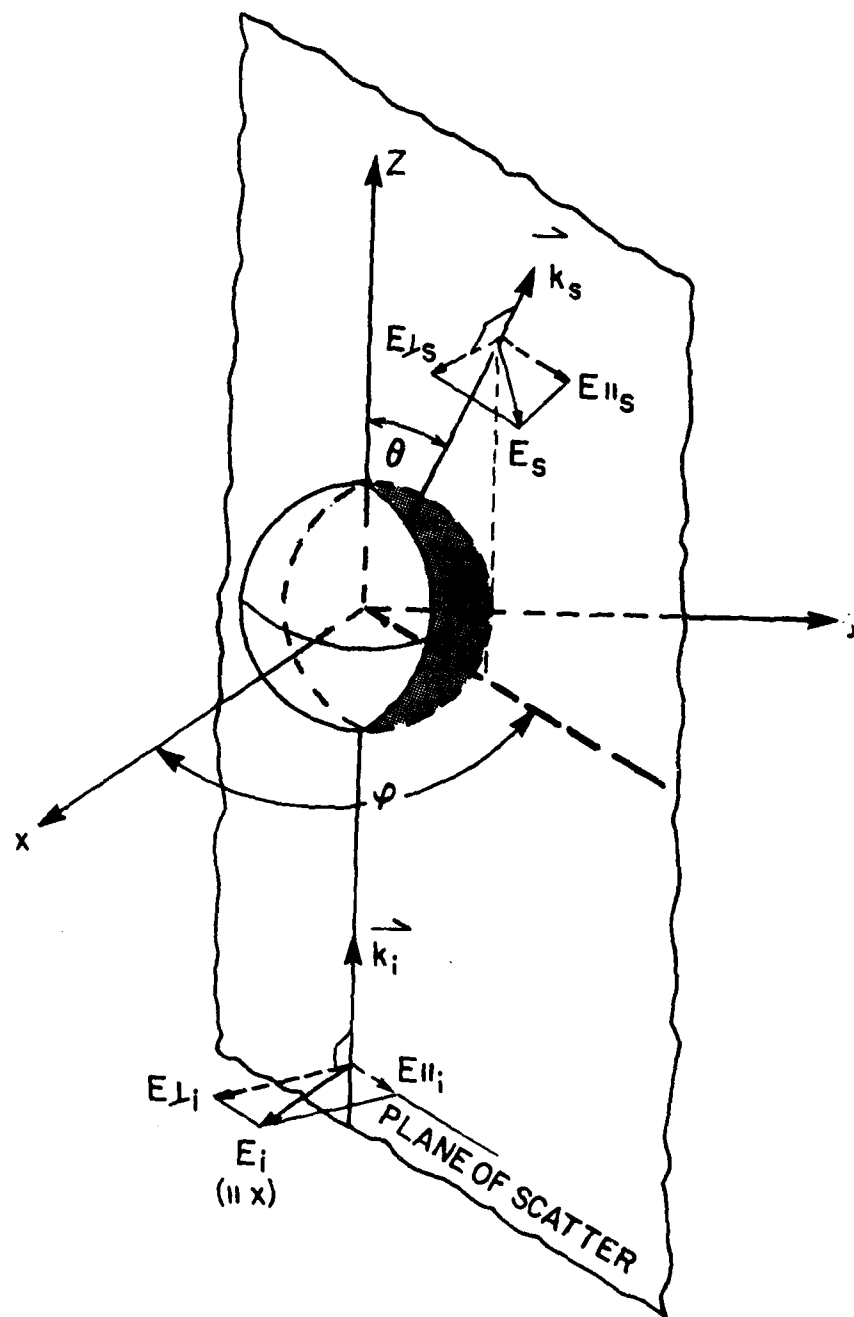


Figure 1. A Physical Representation of the Electromagnetic Radiation Scattered by a Particle.

electric field can be decomposed into two components: E_{\perp} and E_{\parallel} which are perpendicular and parallel to the plane, respectively. Note that the magnitudes of these components are a function of the polar angle ϕ which is formed by the x-axis and the projection of \vec{k}_s on the xy-plane. Further note that since ϕ depends on the orientation of the plane of scatter, the magnitudes of the perpendicular and parallel components of the incident radiation also vary with the orientation of the plane of scatter.

The desired result of the Mie theory is an expression for the electric field scattered by the particle. In its simplest and most general form, the equation can be written as

$$\begin{pmatrix} E_{\parallel,s} \\ E_{\perp,s} \end{pmatrix} = \frac{e^{ik(r-z)}}{-ikr} \begin{bmatrix} S_2(\theta) & S_3(\theta) \\ S_4(\theta) & S_1(\theta) \end{bmatrix} \begin{pmatrix} E_{\parallel,i}(\phi) \\ E_{\perp,i}(\phi) \end{pmatrix}. \quad (11)$$

where $[S]$ is the amplitude scattering matrix consisting of complex numbers. As will be seen, this matrix is governed by the properties and geometry of the particle, and the azimuthal angle of scatter.

In application, the intensity, I , of the electric field is measured. Thus, the incident and scattered electromagnetic radiation are frequently described by the Stokes Parameters I , Q , U , and V , which are defined below:

$$I = \frac{k}{2\omega\mu} [E_{\parallel}E_{\parallel}^* + E_{\perp}E_{\perp}^*]$$

$$Q = \frac{k}{2\omega\mu} [E_{\parallel}E_{\parallel}^* - E_{\perp}E_{\perp}^*]$$

$$U = \frac{k}{2\omega\mu} [E_{\parallel}E_{\perp}^* + E_{\perp}E_{\parallel}^*]$$

$$V = \frac{ik}{2\omega\mu} [E_{\parallel}E_{\perp}^* - E_{\perp}E_{\parallel}^*].$$

(12)

With the aid of Equation (11) and following the notation of Reference 4, the scattered radiation can be characterized in terms of the incident radiation by

$$\begin{pmatrix} I_s \\ Q_s \\ U_s \\ V_s \end{pmatrix} = \frac{1}{k^2 r^2} \begin{bmatrix} S_{11} & S_{12} & S_{13} & S_{14} \\ S_{21} & S_{22} & S_{23} & S_{24} \\ S_{31} & S_{32} & S_{33} & S_{34} \\ S_{41} & S_{42} & S_{43} & S_{44} \end{bmatrix} \begin{pmatrix} I_i \\ Q_i \\ U_i \\ V_i \end{pmatrix} \quad (13)$$

where

$$S_{11} = \frac{1}{2} (|S_1|^2 + |S_2|^2 + |S_3|^2 + |S_4|^2)$$

$$S_{12} = \frac{1}{2} (|S_2|^2 - |S_1|^2 + |S_4|^2 - |S_3|^2)$$

$$S_{13} = \text{Re}\{S_2 S_3^* + S_1 S_4^*\}$$

$$S_{14} = \text{Im}\{S_2 S_3^* - S_1 S_4^*\}$$

$$S_{21} = \frac{1}{2} (|S_2|^2 - |S_1|^2 - |S_4|^2 + |S_3|^2)$$

$$S_{22} = \frac{1}{2} (|S_2|^2 + |S_1|^2 - |S_4|^2 - |S_3|^2)$$

$$S_{23} = \text{Re}\{S_2 S_3^* - S_1 S_4^*\}$$

$$S_{24} = \text{Im}\{S_2 S_3^* + S_1 S_4^*\}$$

$$S_{31} = \text{Re}\{S_2 S_4^* + S_1 S_3^*\}$$

$$S_{32} = \text{Re}\{S_2 S_4^* - S_1 S_3^*\}$$

$$S_{33} = \text{Re}\{S_1 S_2^* + S_3 S_4^*\}$$

$$S_{34} = \text{Im}\{S_2 S_1^* + S_4 S_3^*\}$$

$$S_{41} = \text{Im}\{S_2^* S_4 + S_3^* S_1\}$$

$$S_{42} = \text{Im}\{S_2^* S_4 - S_3^* S_1\}$$

$$S_{43} = \text{Im}\{S_1 S_2^* - S_3 S_4^*\}$$

$$S_{44} = \text{Re}\{S_1 S_2^* - S_3 S_4^*\} . \quad (14)$$

Therefore, the scattered electric field and scattered intensity can be described if $S_1(\theta)$, $S_2(\theta)$, $S_3(\theta)$, and $S_4(\theta)$ are found. These values are found by solving the wave equation. However, the search is simplified by knowing that for homogeneous spherical particles $S_3(\theta) = S_4(\theta) = 0$. Thus, the scattered electric field is

$$\vec{E}_s = \frac{e^{ik(r-z)}}{-ikr} [S_1(\theta) E_{\perp,1}(\phi) \hat{a}_{\perp,1} + S_2(\theta) E_{\parallel,1}(\phi) \hat{a}_{\parallel,1}] , \quad (15)$$

and the scattered intensity is simply

$$I_s = \frac{1}{k^2 r^2} [|S_1(\theta)|^2 I_{\perp,1} + |S_2(\theta)|^2 I_{\parallel,1}] . \quad (16)$$

To begin the search, the wave equation must be written in spherical coordinates since spherical particles are considered. Unlike the position vectors in the Cartesian coordinate system, the position vectors \hat{a}_r , \hat{a}_θ , and \hat{a}_ϕ are not fixed. Thus, the components of \vec{E} separately will not satisfy the scalar wave equation

$$\nabla^2 \psi + k^2 \psi = 0. \quad (17)$$

However, as will be seen, the solution of the scalar wave equation is useful in finding a solution to the vector wave equation. The solutions of ψ can be shown to be

$$\begin{aligned} \psi_{eln} &= \cos l\phi P_n^l(\cos\theta) Z_n(kr) \\ \psi &= \psi_{oln} = \sin l\phi P_n^l(\cos\theta) Z_n(kr) . \end{aligned} \quad (18)$$

where subscripts e and o refer to the even and odd solutions of the function ψ ,

integers $n \geq l \geq 0$,

P_n^l is the associated Legendre polynomial of the first kind of degree n and order l ,

Z_n is one of the spherical Bessel functions listed below:

$$\begin{aligned} j_n(kr) &= \left(\frac{\pi}{2kr}\right)^{1/2} J_{n+1/2}(kr) && \text{spherical Bessel function of the first kind,} \\ y_n(kr) &= \left(\frac{\pi}{2kr}\right)^{1/2} Y_{n+1/2}(kr) && \text{spherical Bessel function of the second kind,} \\ h_n^{(1)}(kr) &= j_n(kr) + iy_n(kr) && \text{spherical Hankel function of the first kind,} \\ h_n^{(2)}(kr) &= j_n(kr) - iy_n(kr) && \text{spherical Hankel function of the second kind.} \end{aligned}$$

The transformation which permits the solution of the vector wave equation via the scalar wave equation is

$$\vec{M} = \nabla \times (\vec{r}\psi). \quad (19)$$

where $\vec{r} = r\hat{a}_r$. The scalar wave equation, shows that this transformation satisfies the vector wave equation because

$$\nabla^2 \vec{M} + k^2 \vec{M} = \nabla \times [\vec{r}(\nabla^2 \psi + k^2 \psi)] = 0. \quad (20)$$

Also, like the electric and magnetic field, the divergence of the vector \vec{M} is zero because the divergence of a curl of any vector is always zero. Furthermore, \vec{M} is coupled to another vector \vec{N} by

$$\begin{aligned}\nabla \times \vec{N} &= k\vec{M} \\ \nabla \times \vec{M} &= k\vec{N}.\end{aligned}\tag{21}$$

The two solutions of \vec{M} can be expressed in terms of the even and odd functions of ψ :

$$\begin{aligned}\vec{M}_{eln} &= \nabla \times \vec{r} \psi_{eln} \\ \vec{M}_{oln} &= \nabla \times \vec{r} \psi_{oln}.\end{aligned}\tag{22}$$

Likewise, the two solutions of \vec{N} can be expressed in terms of \vec{M}_{eln} and \vec{M}_{oln} :

$$\begin{aligned}\vec{N}_{eln} &= \frac{\nabla \times \vec{M}_{eln}}{k} \\ \vec{N}_{oln} &= \frac{\nabla \times \vec{M}_{oln}}{k}.\end{aligned}\tag{23}$$

Reference 4 defines \vec{M} and \vec{N} as vector harmonics and point out that both have the qualities of an electromagnetic field--that is, both satisfy the vector wave equation, both have a zero divergence, and both have curls which are proportional to each other. Since these vector harmonics are mutually orthogonal, they are useful in obtaining an expression for the incident electric field. The electric field can now be written as an expansion in terms of the vector harmonics:

$$\vec{E}_i = \sum_{l=0}^{\infty} \sum_{n=l}^{\infty} (B_{eln} \vec{M}_{eln} + B_{oln} \vec{M}_{oln} + A_{eln} \vec{N}_{eln} + A_{oln} \vec{N}_{oln}),\tag{24}$$

where

$$\vec{M}_{eln} = -l \sin l\phi \frac{P_n^l(\cos\theta)}{\sin\theta} Z_n(kr) \hat{a}_\theta - \cos l\phi \frac{dP_n^l(\cos\theta)}{d\theta} Z_n(kr) \hat{a}_\phi$$

$$\vec{M}_{oln} = l \cos l\phi \frac{P_n^l(\cos\theta)}{\sin\theta} Z_n(kr) \hat{a}_\theta - \sin l\phi \frac{dP_n^l(\cos\theta)}{d\theta} Z_n(kr) \hat{a}_\phi$$

$$\vec{N}_{eln} = n(n+1) \cos l\phi P_n^l(\cos\theta) \frac{Z_n(kr)}{kr} \hat{a}_r$$

$$+ \cos l\phi \frac{dP_n^l(\cos\theta)}{d\theta} \frac{1}{kr} \frac{d[kr Z_n(kr)]}{d(kr)} \hat{a}_\theta$$

$$- l \sin l\phi \frac{P_n^l(\cos\theta)}{\sin\theta} \frac{1}{kr} \frac{d[kr Z_n(kr)]}{d(kr)} \hat{a}_\phi$$

(25)

$$\vec{N}_{oln} = n(n+1) \sin l\phi P_n^l(\cos\theta) \frac{Z_n(kr)}{kr} \hat{a}_r$$

$$+ \sin l\phi \frac{dP_n^l(\cos\theta)}{d\theta} \frac{1}{kr} \frac{d[kr Z_n(kr)]}{d(kr)} \hat{a}_\theta$$

$$+ l \cos l\phi \frac{P_n^l(\cos\theta)}{\sin\theta} \frac{1}{kr} \frac{d[kr Z_n(kr)]}{d(kr)} \hat{a}_\phi.$$

A_{eln} , A_{oln} , B_{eln} , and B_{oln} are coefficients whose values are derived from orthogonality conditions of the inner products of (E_i, M_{eln}) , $(M_{eln}, M_{el'n'})$, (E_i, M_{oln}) , $(M_{oln}, M_{ol'n'})$, (E_i, N_{eln}) , $(N_{eln}, N_{el'n'})$, (E_i, N_{oln}) , and $(N_{oln}, N_{ol'n'})$.

For the incident linearly polarized plane wave,

$$\begin{aligned} \vec{E}_i &= E_0 e^{i(kz - \omega t)} \hat{a}_x \\ &= E_0 e^{i(kr \cos\theta - \omega t)} (\sin\theta \cos\phi \hat{a}_r + \cos\theta \cos\phi \hat{a}_\theta - \sin\phi \hat{a}_\phi), \end{aligned} \quad (26)$$

the resulting values of these coefficients are as follows:

$$A_{e1n} = A_{e1n} = -iE_0 \frac{i^n(2n+1)}{n(n+1)} = -B_{o1n},$$

$$A_{o1n} = 0,$$
(27)

$$B_{e1n} = 0,$$

$$B_{o1n} = B_{o1n} = E_0 \frac{i^n(2n+1)}{n(n+1)}.$$

Only nonzero coefficients are obtained from orthogonality conditions when $l=1$. Thus, the expansion of the incident electric field in spherical harmonics is

$$\vec{E}_i = E_0 \sum_{n=1}^{\infty} i^n \frac{2n+1}{n(n+1)} [\vec{M}_{o1n} - i\vec{N}_{e1n}].$$
(28)

Since the magnetic field is coupled to the electric field by Faraday's law, $\vec{H} = -i(\nabla \times \vec{E})/\omega\mu$, the incident magnetic field can be found by applying Equations (21) and (23) to the expression for the incident electric field to obtain

$$\vec{H}_i = -\frac{k}{\omega\mu} E_0 \sum_{n=1}^{\infty} i^n \frac{2n+1}{n(n+1)} (\vec{M}_{e1n} + i\vec{N}_{o1n}).$$
(29)

Expressions for the internal and scattered field follow from these expansions. Following the notation of Reference 4, the field within the particle is written as

$$\vec{E}_p = E_0 \sum_{n=1}^{\infty} i^n \frac{2n+1}{n(n+1)} (c_n \vec{M}_{o1n} - id_n \vec{N}_{e1n})$$

$$\vec{H}_p = -\frac{kp}{\omega\mu} E_0 \sum_{n=1}^{\infty} i^n \frac{2n+1}{n(n+1)} (d_n \vec{M}_{e1n} + ic_n \vec{N}_{o1n}). \quad (30)$$

Likewise, the scattered field is expressed by

$$\begin{aligned} \vec{E}_s &= E_0 \sum_{n=1}^{\infty} i^n \frac{2n+1}{n(n+1)} (-b_n \vec{M}_{o1n,h} + ia_n \vec{N}_{e1n,h}) \\ \vec{H}_s &= \frac{k}{\omega\mu} E_0 \sum_{n=1}^{\infty} i^n \frac{2n+1}{n(n+1)} (a_n \vec{M}_{e1n,h} + ib_n \vec{N}_{o1n,h}). \end{aligned} \quad (31)$$

The coefficients a_n , b_n , c_n , d_n are found by applying boundary conditions for a perfect dielectric (Appendix A 8a-b) to the fields tangential to the particle's surface, namely (E_θ, H_θ) and (E_ϕ, H_ϕ) . Thus, it is assumed that no net free charge is present on the particle's surface. If the magnetic permeability of the particle is also assumed to be equivalent to that of the surrounding medium, the expression for the coefficients can be simplified to

$$\begin{aligned} a_n &= \frac{\psi'_n(y)\psi_n(x) - m\psi_n(y)\psi'_n(x)}{\psi'_n(y)\xi_n(x) - m\psi_n(y)\xi'_n(x)} \\ b_n &= \frac{m\psi'_n(y)\psi_n(x) - \psi_n(y)\psi'_n(x)}{m\psi'_n(y)\xi_n(x) - \psi_n(y)\xi'_n(x)} \\ c_n &= \frac{m\psi_n(x)\xi'_n(x) - m\xi_n(x)\psi'_n(x)}{\psi_n(y)\xi'_n(x) - m\xi_n(x)\psi'_n(y)} \\ d_n &= \frac{m\psi_n(x)\xi'_n(x) - m\xi_n(x)\psi'_n(x)}{m\psi_n(y)\xi'_n(x) - \xi_n(x)\psi'_n(y)}, \end{aligned} \quad (32)$$

where $\psi_n(\rho) = \rho j_n(\rho)$

$$\begin{aligned} \xi_n(\rho) &= \rho h_n^{(1)}(\rho) \\ x &= k_0 a = 2\pi a / \lambda_0, \\ y &= ka, \end{aligned}$$

$$k = mk_0,$$

a = radius of the particle.

The vector harmonics are written as

$$\vec{M}_{ein} = -\sin\phi \Pi_n(\cos\theta) Z_n(k_m r) \hat{a}_\theta - \cos\phi \tau_n(\cos\theta) Z_n(k_m r) \hat{a}_\phi$$

$$\vec{M}_{oin} = \cos\phi \Pi_n(\cos\theta) Z_n(k_m r) \hat{a}_\theta - \sin\phi \tau_n(\cos\theta) Z_n(k_m r) \hat{a}_\phi$$

$$\begin{aligned} \vec{N}_{ein} = & n(n+1) \cos\phi \sin\theta \Pi_n(\cos\theta) \frac{Z_n(k_m r)}{k_m r} \hat{a}_r \\ & + \cos\phi \tau_n(\cos\theta) \frac{1}{kr} \frac{d[k_m r Z_n(k_m r)]}{d(k_m r)} \hat{a}_\theta \end{aligned} \quad (33)$$

$$- \sin\phi \Pi_n(\cos\theta) \frac{1}{k_m r} \frac{d[k_m r Z_n(k_m r)]}{d(k_m r)} \hat{a}_\phi$$

$$\vec{N}_{oin} = n(n+1) \sin\phi \sin\theta \Pi_n(\cos\theta) \frac{Z_n(k_m r)}{k_m r} \hat{a}_r$$

$$+ \sin\phi \tau_n(\cos\theta) \frac{1}{k_m r} \frac{d[k_m r Z_n(k_m r)]}{d(k_m r)} \hat{a}_\theta$$

$$+ \cos\phi \Pi_n(\cos\theta) \frac{1}{k_m r} \frac{d[k_m r Z_n(k_m r)]}{d(k_m r)} \hat{a}_\phi$$

$$\text{where } \Pi_n(\cos\theta) = \frac{dP_n(\cos\theta)}{\sin\theta d(\cos\theta)} = \frac{P'_n(\cos\theta)}{\sin\theta},$$

$$\tau_n(\cos\theta) = \frac{d}{d\theta} \frac{dP_n(\cos\theta)}{d(\cos\theta)} = \frac{d}{d\theta} P'_n(\cos\theta),$$

$k_m = k$ of the particular medium where the electromagnetic propagation is considered,

r = distance from the particle center.

For considering the electromagnetic fields incident on and within the particle, the appropriate spherical Bessel function used in the expressions for \vec{M} and \vec{N} is $j_n(k_m r)$ because the fields are finite at the origin (the center of the particle). For the scattered electromagnetic field the appropriate spherical Bessel function describing an outgoing spherical wavefront is the spherical Hankel function of the first kind, $h_n^{(1)}(k_m r)$; thus, the subscript h is present in the expression for the scattered field.

Furthermore, for large distances from the particle ($k_m r \gg n^2$), the spherical Hankel function is approximated as

$$h_n^{(1)}(kr) = \frac{(-i)^n e^{ikr}}{ikr}, \quad (34)$$

The use of this approximation leads to a $(kr)^2$ term in the denominator of the radial component of the scattered electromagnetic wave. Therefore, at large distances from the particle, the scattered radial field can then be neglected.

By substituting all the appropriate functions into the expression for the scattered electric field, simplified expressions for the components are obtained:

$$E_{s,\theta} = E_{s,\parallel} = e^{-i\omega t} \frac{E_0 \cos\phi e^{ik_m r}}{-ik_m r} \sum_{n=1}^{\infty} \frac{(2n+1)}{n(n+1)} (a_n \tau_n + b_n \pi_n) \quad (35)$$

$$E_{s,\phi} = E_{s,\perp} = -e^{-i\omega t} \frac{E_0 \sin\phi e^{ik_m r}}{-ik_m r} \sum_{n=1}^{\infty} \frac{(2n+1)}{n(n+1)} (a_n \pi_n + b_n \tau_n)$$

However, early in the derivation, the polarization of the incident radiation was assumed to be along the x-axis. As a result, the parallel and perpendicular components of the incident electric field can be written as

$$E_{\parallel,i} = E_0 \cos\phi e^{i(kz - \omega t)} \quad (36)$$

$$E_{\perp,i} = -E_0 \sin\phi e^{i(kz - \omega t)}.$$

With these equations, the final expression of the scattered electric field is obtained:

$$E_{s,\theta} = E_{s,\parallel} = \frac{E_{\parallel,i} e^{ik(r-z)}}{-ikr} \sum_{n=1}^{\infty} \frac{(2n+1)}{n(n+1)} (a_n \tau_n + b_n \pi_n) \quad (37)$$

$$E_{s,\phi} = E_{s,\perp} = \frac{E_{\perp,i} e^{ik(r-z)}}{-ikr} \sum_{n=1}^{\infty} \frac{(2n+1)}{n(n+1)} (a_n \pi_n + b_n \tau_n) .$$

Thus, for spherical particles, the search for the elements of the matrix [S] is complete. By comparing the final result with Equation (11), and by remembering $S_3(\theta) = S_4(\theta) = 0$ for spherical particles, it can be seen that

$$S_1(\theta) = \sum_{n=1}^{\infty} \frac{2n+1}{n(n+1)} (a_n \pi_n + b_n \tau_n) \quad (38)$$

$$S_2(\theta) = \sum_{n=1}^{\infty} \frac{2n+1}{n(n+1)} (a_n \tau_n + b_n \pi_n) .$$

Consider, for example, the case of scattering in the $\phi = 90^\circ$ plane (yz-plane). In this circumstance, the incident radiation is perpendicularly polarized with respect to the plane of scatter. From the previous equation, the scattered intensity is then

$$I_s = \frac{1}{k^2 r^2} (|S_1|^2 I_{\perp,i}) . \quad (39)$$

In Figures 2 and 3, the common logarithm of this scattered intensity normalized by the factor, $I_0/k^2 r^2$, is plotted against the azimuthal angle θ for various particle sizes and two refractive indices. In these diagrams, light is incident at $\theta = 180^\circ$; thus, backscatter occurs for $\theta = 180^\circ$ and forward scatter occurs for $\theta = 0^\circ$. Figure 2 is obtained by assuming a real refractive index while Figure 3 shows the intensity profile when the refractive index is a complex number. As can be seen from comparing Figures 2c and 3c, the presence of the imaginary part in the refractive index is responsible for the damping or attenuation of the electromagnetic wave. Through a comparison of the intensity profiles for each particle it can also be seen that as the particle size increases, the forward scatter lobe becomes narrower and the magnitude of the forward scattered light increases.

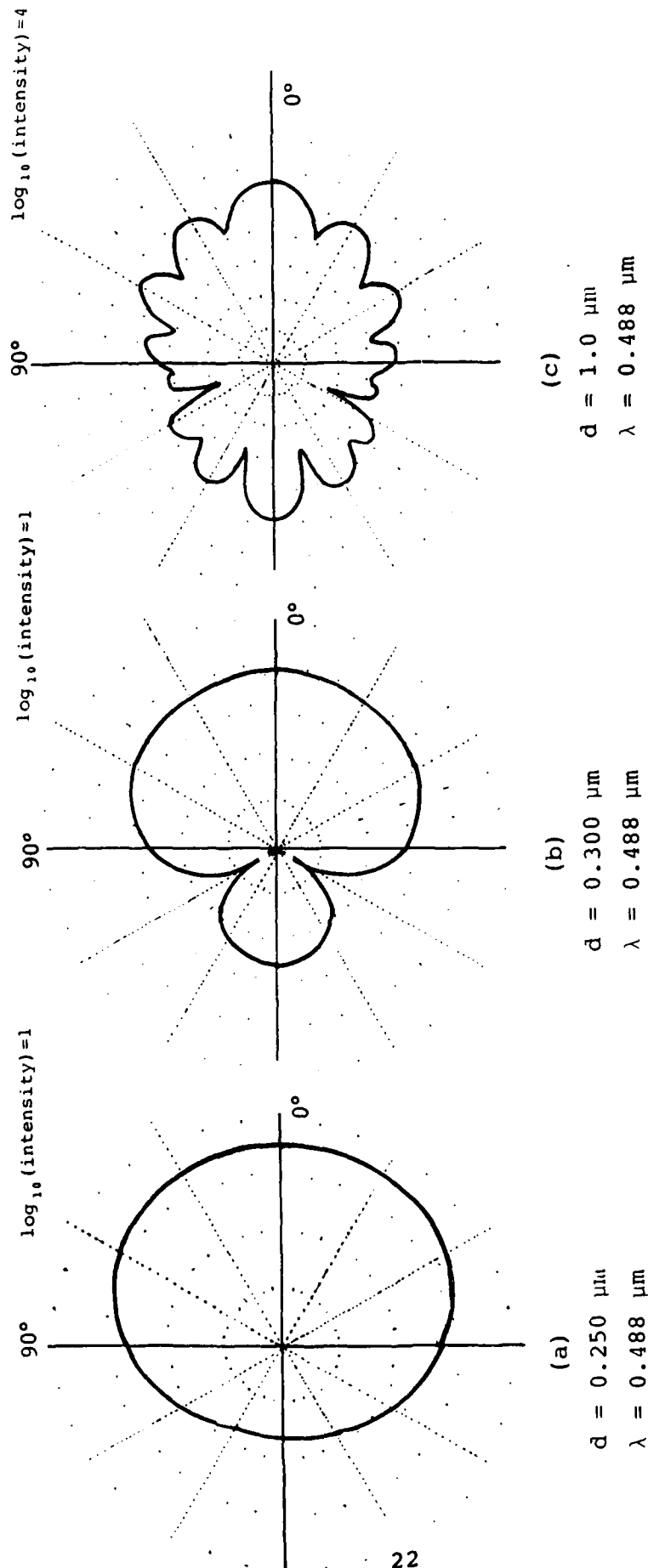


Figure 2. Polar Plots of the Common Logarithm of the Ratio of Scattered Intensity to Incident Intensity for Particles of Various Sizes and Refractive Index $1.57 - i0.0$.

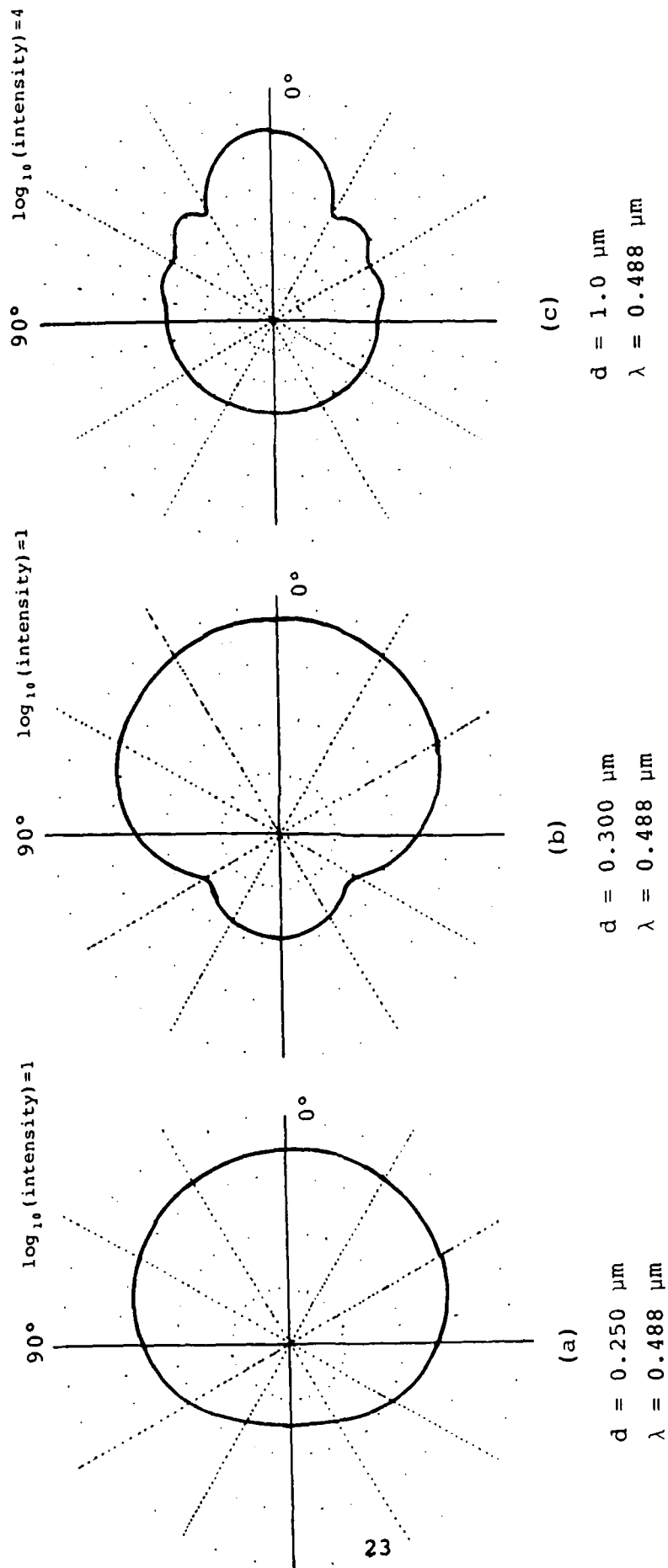


Figure 3. Polar Plots of the Common Logarithm of the Ratio of Scattered Intensity to Incident Intensity for Particles of Various Sizes and Refractive Index $1.57 - i0.56$.

In some circumstances (i.e., particle sizing measurements in combustion environments), the incident intensity may be unknown and difficult to measure. This unknown parameter presents a problem if other quantities such as particle size are also unknown. However, this problem can be circumvented by taking the ratio of the scattered intensities collected at two different angles of scatter. Mathematically, for linearly polarized light perpendicular to the plane of scatter with ϕ fixed at 90° , the result is an equation relating the intensity ratio to particle size:

$$I_{\text{ratio}} = \frac{I_{s,A}}{I_{s,B}} = \frac{|S_1(\theta_A)|^2}{|S_1(\theta_B)|^2} \quad (40)$$

Plots of intensity ratio versus particle size for a fixed angle pair and refractive index are shown in Figures 4a and 4b. Note that for a complex refractive index, the curve is relatively well-behaved; monotonically decreasing for increasing particle size. However, this behavior is not seen for a real refractive index. Although a given particle size corresponds to a specific intensity ratio, the converse is not true. This multiplicity does not pose a serious problem in determining particle size if it is remembered that at near forward scattering angles, the absolute scattered intensity increases with increasing particle size. As a result, provisions must be made in the electronics of Mie theory-based instrumentation to allow the discrimination of different size particles having the same intensity ratio. One specific size discrimination scheme is discussed in the next section.

Many computer codes (References 4, 6, and 7) are available which calculate the scattered intensity. However, it is important to note that the expressions shown are only point expressions for the scattered field. In practical situations, the scattered radiation is collected over a finite solid angle. Mathematically, this measurement translates into the problem of finding the total scattered intensity at various planes of scatter. In other words, the point values must be integrated over the desired solid angle. As can be seen by the complexity of the Mie expression, a numerical integration scheme must be implemented.

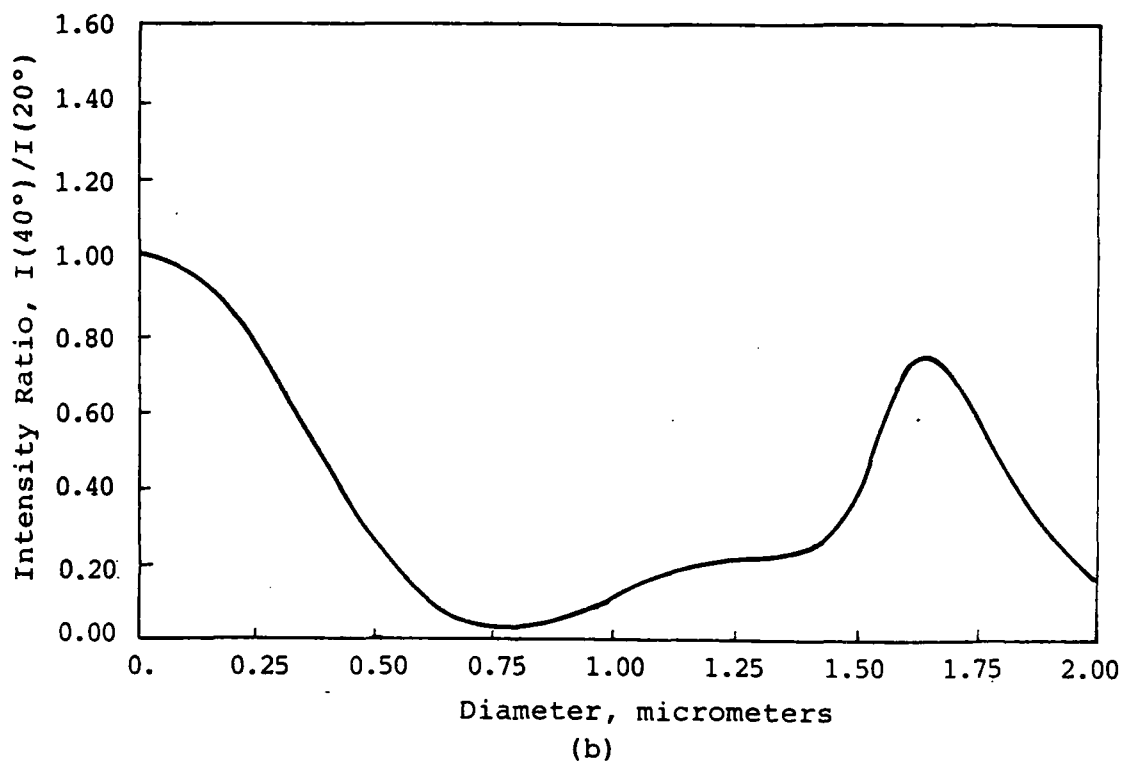
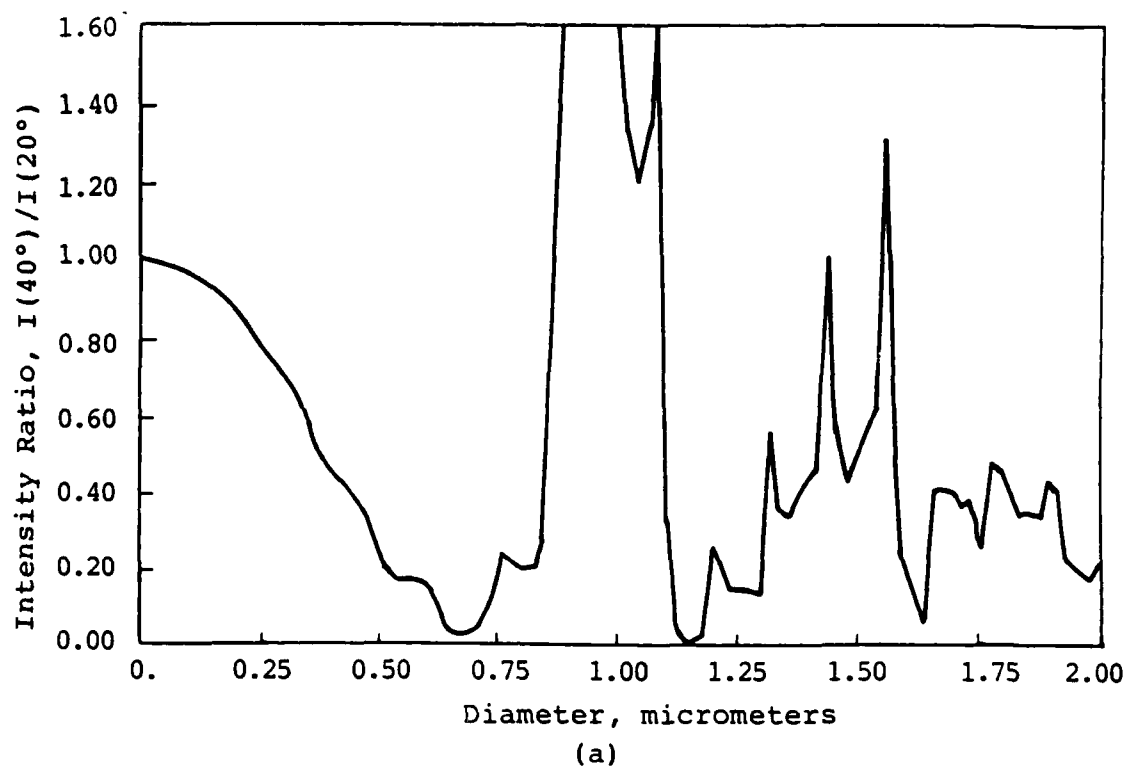


Figure 4. Plots of Intensity Ratio Versus a Wide Range of Particle Sizes for Angle Pair 40°/20° and Wavelength 0.488 μm . For (a), the refractive index is 1.57 - i0.0. For (b), the refractive index is 1.57 - i0.56.

SECTION III

THE INTEGRATED PARTICLE SIZING SYSTEM

The instrumentation used for nonintrusive measurement of particle diameters in hostile environments is composed of an optical system, a data processing unit, and a data management system. To test and calibrate the system, a particle generation system for known particle sizes is also necessary. In the following pages, each component is discussed, as well as the calibration and practical application of the instrument.

A. OPTICAL SYSTEM

The Integrated Particle Sizing System (SDL Model IPSS-200), designed by Spectron Development Laboratories, Inc. (Costa Mesa, California), to measure the formation, growth, and destruction of soot particulates in flames, has a large measurement range with the incorporation of two techniques for particle sizing: scattered intensity ratioing for particle diameters between 0.08 and 3.0 μm and particle sizing interferometry for particle diameters between 2.5 and 45 μm . Particle-sizing interferometry is an extension of the laser Doppler velocimeter technique. Scattered intensity ratioing, which forms the ratio of the scattered light collected at two different angles, can be further subdivided into large-angle and small-angle ratioing techniques. The main difference between these two techniques is the configuration of the receiving optics. As described by Spectron, the small-angle technique ($8^\circ/2.5^\circ$, $10^\circ/5^\circ$, and $12^\circ/5^\circ$) uses annular masks to define the separate angles. Large-angle ratioing ($40^\circ/20^\circ$, $50^\circ/20^\circ$, and $60^\circ/20^\circ$) uses a separate set of lenses for each angle of the angle pair. The dynamic range, as reported by Spectron, for the complex refractive index of soot, 1.57-10.56, and the six angle pairs used for the small-angle and large-angle ratioing technique is given in Table 1. Note that for the study of soot formation from gas turbine engines (typically, the soot particles average 0.15 μm in diameter), the large-angle technique is of particular interest. Thus, the large-angle configuration will be described.

A schematic of the IPSS is shown in Figure 5. The incident radiation is

TABLE 1. DYNAMIC RANGE FOR SOOT AS PROPOSED BY SPECTRON.

For 1.57 - 10.56 (soot)

ANGLE PAIR(degrees)	MINIMUM DIAMETER()m	MAXIMUM DIAMETER()m
8°/2.5°	0.45	2.95
10°/5°	0.40	2.44
12°/5°	0.30	1.97
40°/20°	0.12	0.57
50°/20°	0.09	0.45
60°/20°	0.08	0.37

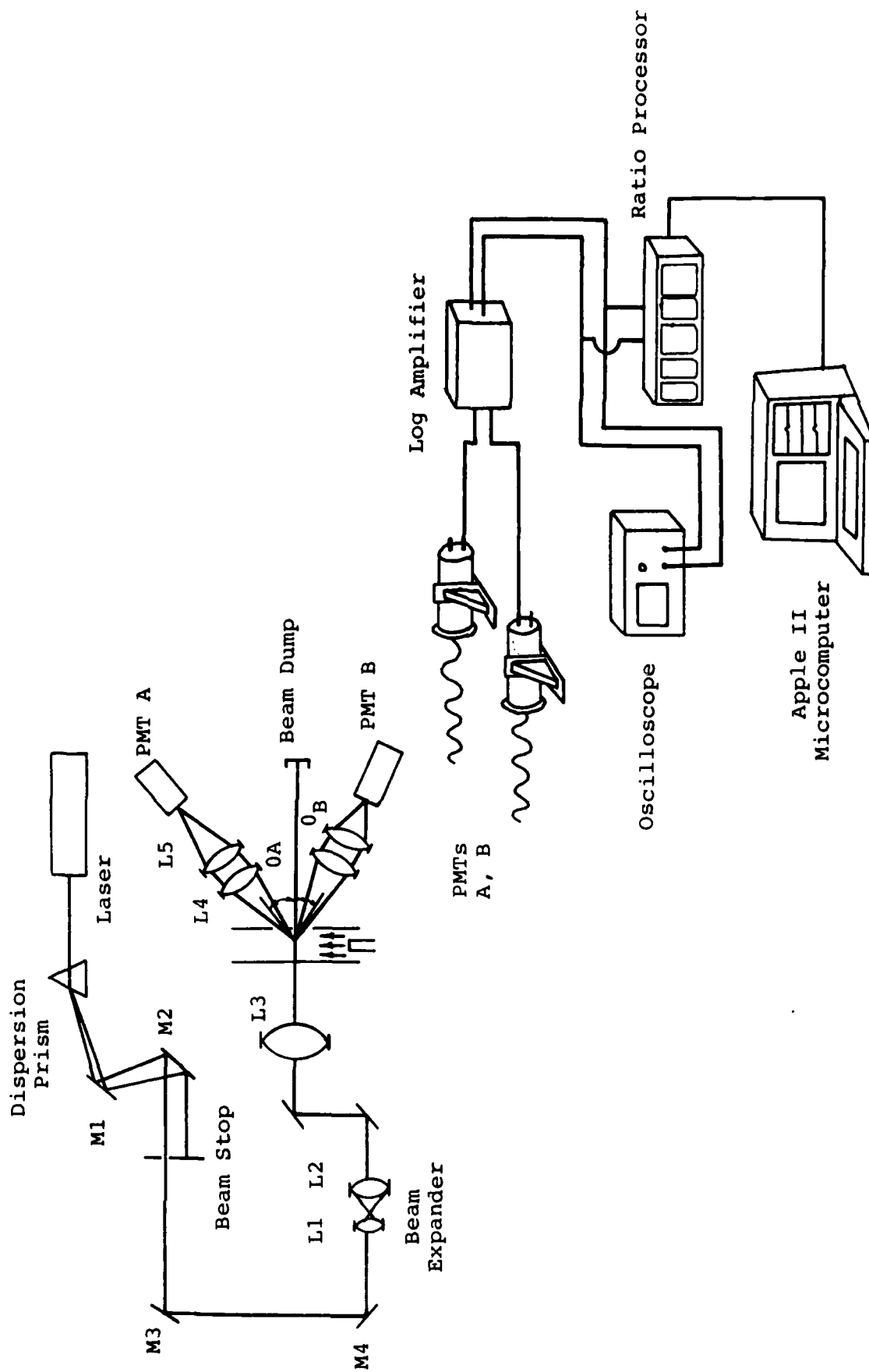


Figure 5. Schematic of the IPSS

supplied by the 0.488 μm line of a 2-Watt Lexel Argon Ion Laser (Model 95) operating in the multiline mode. The various lines are separated by a dispersion prism; however, only the 0.488 μm line is allowed to pass through the system. After reflecting from mirrors M1, M2, M3, and M4, the beam is expanded by a variable beam expander comprised by lenses L1 and L2, which, according to Spectron, has the potential of increasing the beam diameter over a range of 1.7 to 8.3 times its initial size. After expansion, the beam is directed toward the dichroic mirror which ensures that the electric field is linearly polarized. The beam is then focused by an 800 mm lens (L3). The tightly focused beam provides a small sampling volume, good spatial resolution, a high signal-to-noise ratio, and a method of counting particles if only one particle at a time is in the probe volume for each measurement. Thus, if the waist diameter of the focused beam is theoretically related to the beam diameter in the equation,

$$d_{\text{waist}} = 4\lambda f / \pi d_{\text{laser}} \quad (41)$$

where d_{waist} = diameter of the beam at the waist,

d_{laser} = diameter of beam before focusing,

f = focal length of focusing lens,

λ = wavelength of the radiation,

the purpose of beam expansion before focusing is realized.

The radiation scattered by particles entering the probe volume is collected at one of the previously determined angle pairs by lenses L4, L5, L6, and L7 and focused onto photomultiplier tubes PMT A and PMT B (RCA Model 8575). Included in the PMT housings are bandpass filters which have a bandwidth of approximately 2 nm and a transmittance of approximately 20 percent (Figure 6). Power is supplied to the PMTs by a triple-high-voltage power supply (SDL HV-1000) which can operate three PMTs and is capable of generating voltages up to -1000 volts dc at 4 mA. As with all photomultiplier tubes, the amount of light observed at the aperture of the tube is directly

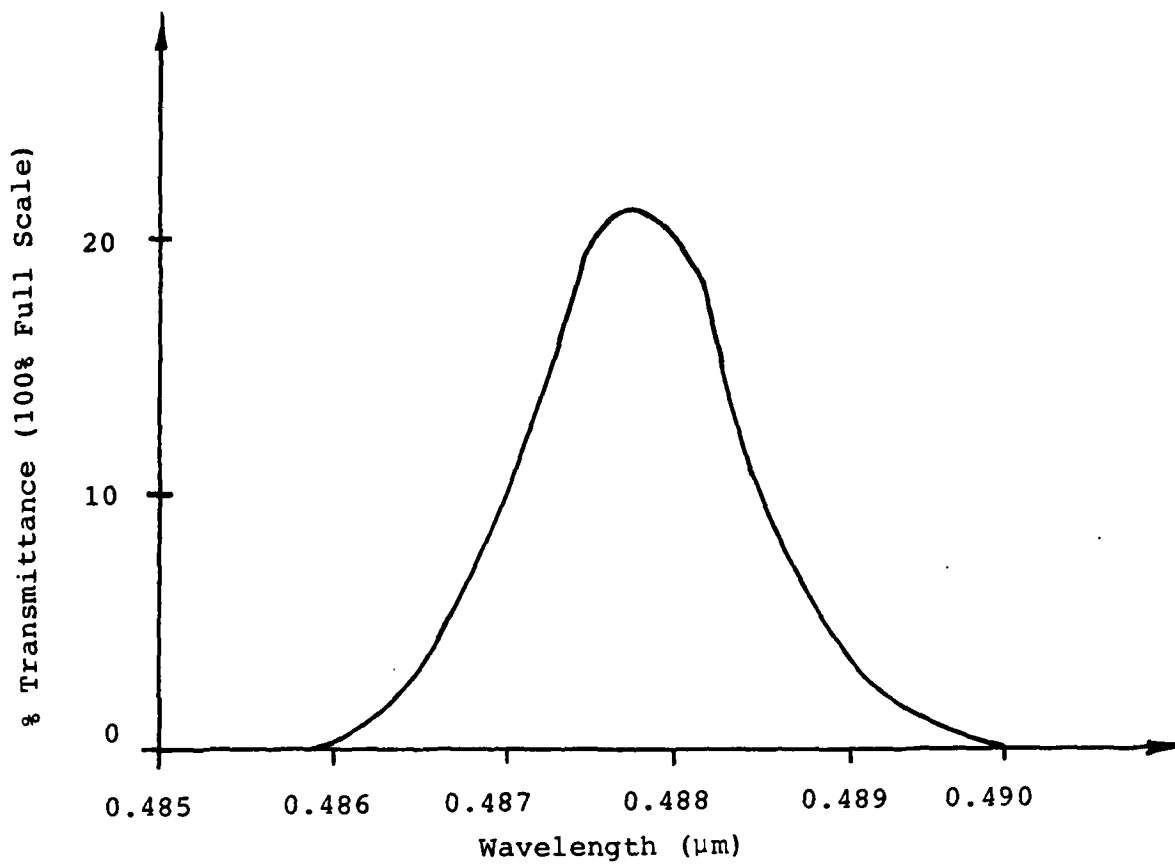


Figure 6. Percent Transmittance versus Wavelength Measurements for PMT Filters.

proportional to the negative output current when operating in the tube's linear current range. The resulting signals from the two PMTs are then sent to the processing units.

B. DATA PROCESSING SYSTEM

The PMT output currents are first passed through a logarithmic amplifier (SDL LA-1000) where they are converted to positive voltages and are scaled by a factor of 2 volts per decade current with an input current of -1 mA producing a 10 volt peak output pulse. In equation form, the relationship can be written as

$$\begin{aligned} v_s &= 2\log(i_s/i_o) \\ \text{where } v_s &= \text{output voltage of the signal,} \\ i_s &= \text{signal current in amperes,} \\ i_o &= 10^{-8} \text{ A.} \end{aligned} \tag{42}$$

The voltage signals are then directed to the ratio processor (SDL RP-1001). Within the processor, several operations take place. First, the signals are passed through a peak detection circuit. A peak is said to occur when the large-angle signal goes above the 1.5-volt threshold value and then decays to a value of 1 volt below its corresponding maximum voltage. The detection circuit is reset when the large-angle signal goes below the 1-volt threshold level. The dc levels of the two peaks are then sent to an analog subtractor circuit which subtracts the large-angle signal (A) from the small-angle signal (B). The resulting signal becomes the common logarithm of the intensity ratio, since

$$v_B - v_A = -2\log(i_A/i_B). \tag{43}$$

The analog subtractor circuit has an output ranging from 0 volt to 2 volts for the ratio i_A/i_B of 1 to 0.1, respectively. The range of the subtractor output is increased to 0 to 10 volts when the signal is passed through an amplifier with a gain of 5. Upon amplification, the output travels to an analog/digital converter where it is converted to an eight-bit binary number. The validity of the data word is internally checked in the processor by examining the eighth bit. Thus, the eighth bit is used as a status bit. As outlined by

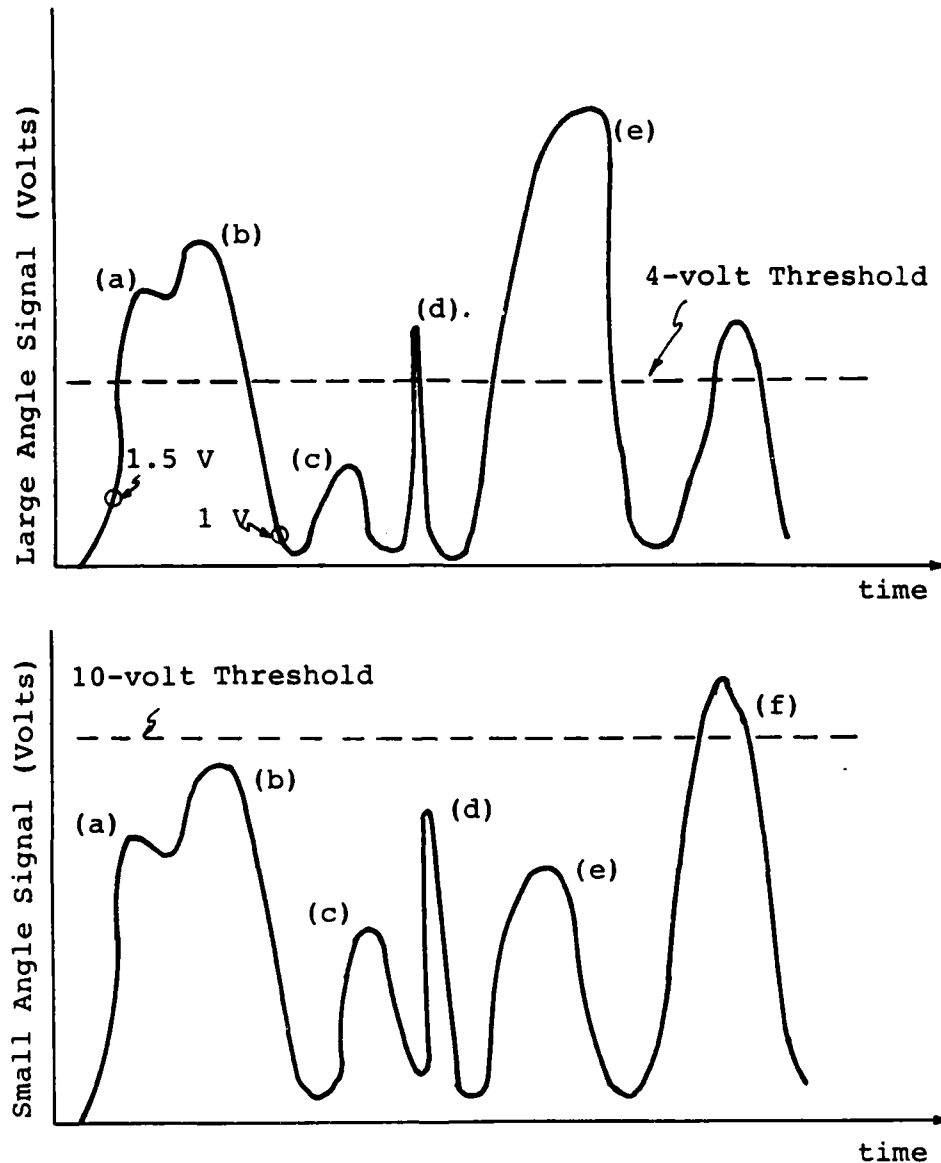


Figure 7. Examples of the Restrictions of Valid and Invalid Data:

- (a) A possible signal, but signal does not deteriorate to 1 volt below the maximum before the next signal arrives. This signal is not recognized by the processor.
- (b) A valid data point.
- (c) The peak signal is less than the large-angle signal of 4 volts (invalid data).
- (d) The pulse width is less than 2 μ sec (invalid data).
- (e) The ratio of the large-angle signal to the small-angle signal is greater than 1.0 (invalid data).
- (f) The peak of the small-angle signal is greater than the small-angle threshold value of 10 volts (invalid data).

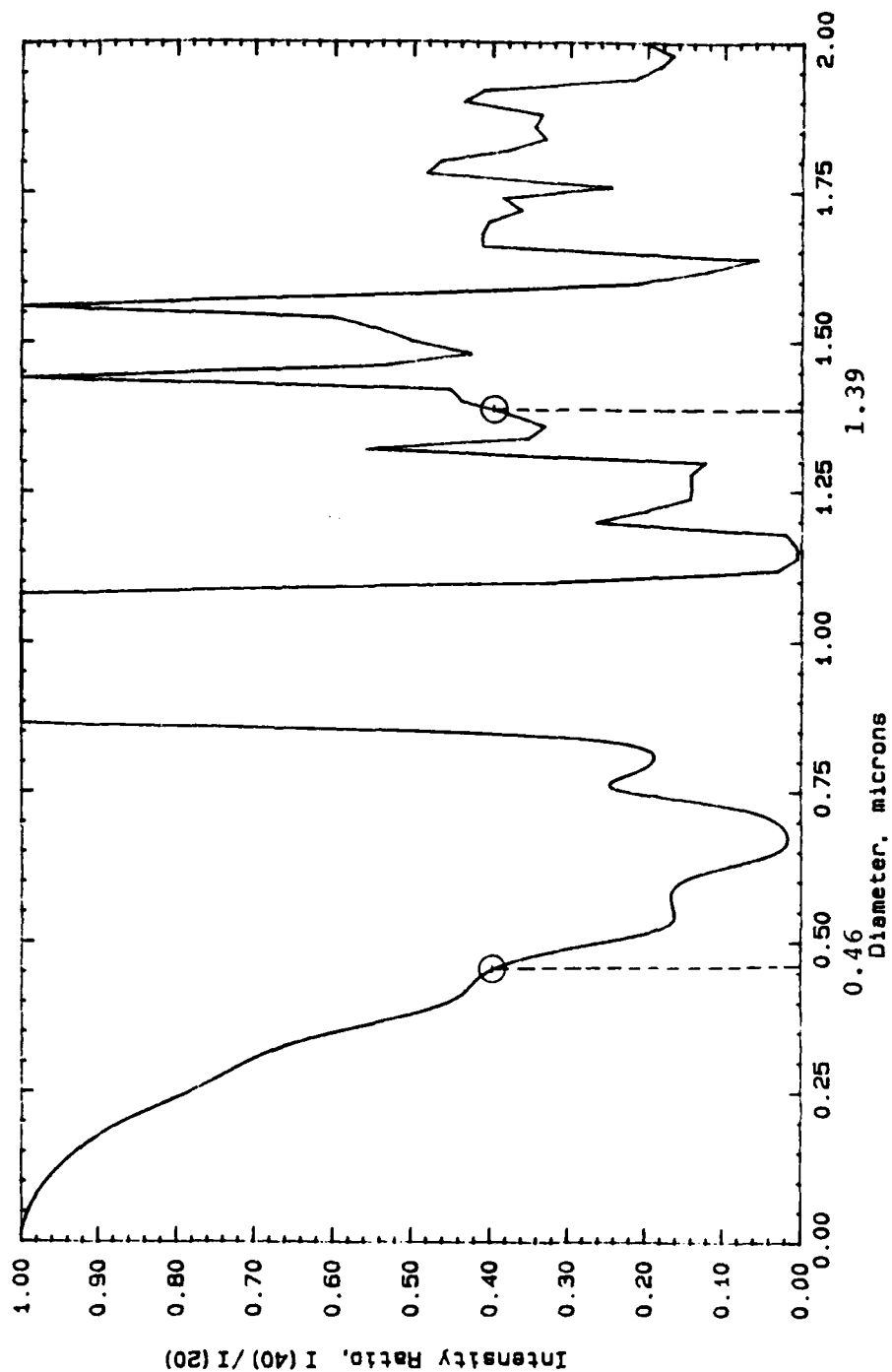


Figure 8. Plot of Intensity Ratio versus Diameter for a 40°/20° Angle Pair and a Real Refractive Index of 1.57.

Both 0.46 μm and 1.39 μm particles have an Intensity ratio of 0.396.

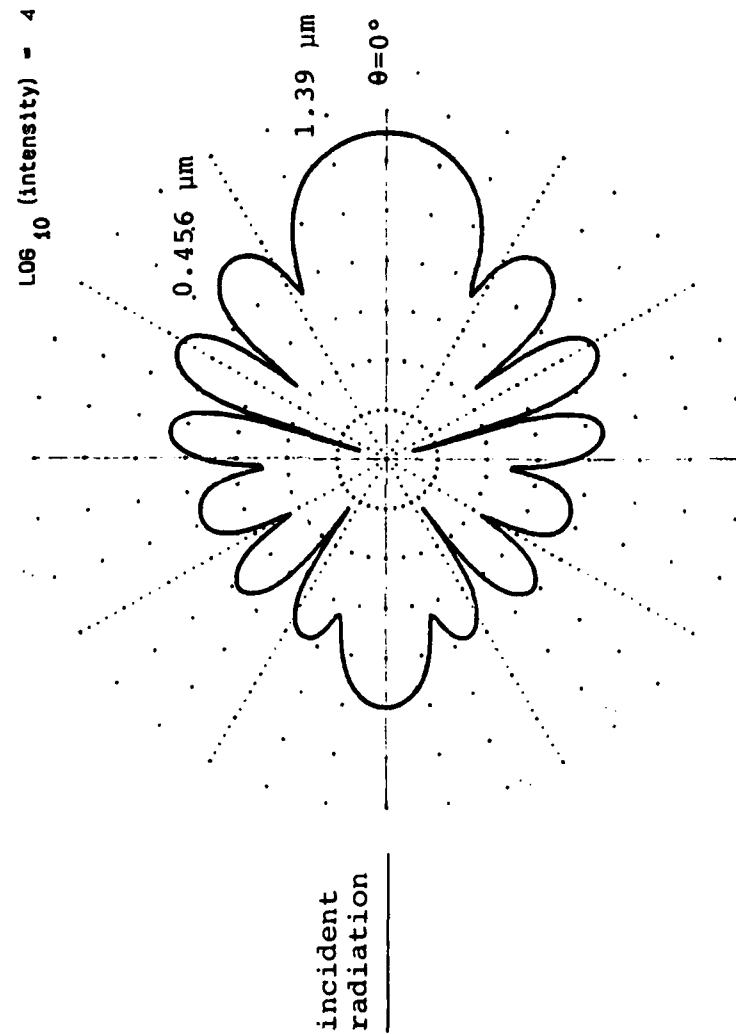


Figure 9. Polar Plots of the Common Logarithm of the Ratio of the Scattered Intensity to Incident Intensity for a $0.456 \mu\text{m}$ and a $1.39 \mu\text{m}$ Particle. (Both particles are assumed to have a refractive index of 1.57. The wavelength of the incident radiation was assumed to be $0.488 \mu\text{m}$.)

Spectron, a data word is considered valid when the following three criteria are met:

1. The input signal level from the small angle must be less than 10 volts. In terms of current, the output of PMT B must be less than 1 mA.
2. The input signal level from the large angle must be greater than a minimum of +4 volts for high speed operation. In terms of current, the output of PMT A must be greater than 1 μ A.
3. The width of the input signal pulse from the large angle must be greater than a minimum of 2 μ sec for high speed operation.

Figure 7 demonstrates these restrictions. As a consequence of Restrictions 1 and 2, a particle size outside the range of a specified angle pair should not be considered as valid data although that size may have an intensity ratio equal to that of a particle inside the angle pair's range. For example, although latex particles of 0.456 μ m and 1.39 μ m have the same intensity ratio at an angle pair of 40°/20° (Figure 8), the absolute scattered intensity for the larger size particle is about 10 times that of the smaller particle (Figure 9). Therefore, if the electronics of the system are properly adjusted, the signal from the large particle is rejected.

C. DATA MANAGEMENT SYSTEM

The digitized data is transferred to an Apple II microcomputer which, with the help of the software package (SDL HG-3001), stores the real-time data in memory and displays a histogram. These histogram results are also stored in tabular form. An example of the data is shown in Figure 10. The intensity ratio range of 0.1 to 1.0 is divided into 64 subintervals or bins according to the equation

$$I_{bin} = 10^{-(N + BIN\#)/64} \quad (44)$$

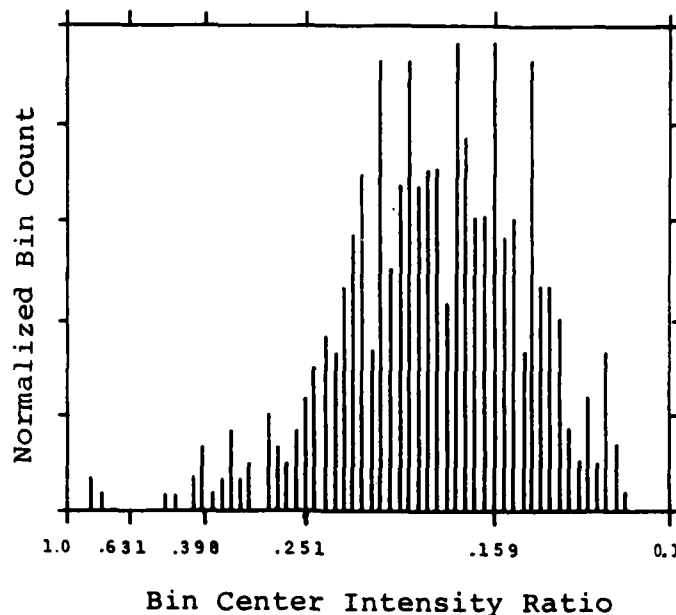
where $N = \begin{cases} 0, & \text{for maximum bin ratio} \\ 1/2, & \text{for bin center ratio} \\ 1, & \text{for minimum bin ratio} \end{cases}$

These ranges are shown in Table 2. Particle sizes are correlated with each bin intensity ratio range by use of bin tables provided in the IPSS software package. Note that only 62 bins are shown in the histogram. Bins 1 through 62 are treated as valid data and are displayed. However, since the ratio processor will accept only those intensity ratios which are less than 1.0 but greater than 0.1, Bin 0 which contains any ratio greater than or equal to 1.0, and Bin 63, which contains any ratio less than or equal to 0.1, are treated as invalid data. The display is limited to 152 data points (counts) in each bin. Data acquisition is terminated when either a bin becomes full, the total number of data samples stored in the histogram exceeds a value set by the operator (limited by the values 10^1 to 10^6), or the operator terminates the procedure. Stored within the table will be the maximum raw count (the maximum count in one bin), the total raw count (the sum of all the counts in the valid bins 1 through 62), and the sampling time. If desired, the linear, surface, volume, and Sauter mean (also known as the mean volume-surface) diameters, as well as the standard deviation, can be calculated. The sample output shown in Figure 10 displays the bin center intensity ratios, its corresponding bin center diameter, and the number of counts in each bin.

Observation of a Tektronix dual-trace oscilloscope (Model 434) and the ratio display and data rate display on the ratio processor panel aid in the real-time monitoring of these signals, as well as in determining whether or not the above criteria are met. The oscilloscope monitors the logarithmic amplifier output and displays the voltage signal of each angle. The intensity ratio display shows the previously calculated ratio at a 1 Hz rate. The presence of large or small particles out of the range of detection is signified by a ratio display of 0.1 or 0.99, respectively. The data rate display, also updated at a 1 Hz rate, indicates in kHz the number of signals read in the previous time interval. A low data rate can indicate that either a low- or high-number density is present. In the latter case, the large-angle signal does not deteriorate to the 1-volt threshold level before another signal peak occurs. By monitoring the signal on the oscilloscope, the operator can determine if either situation is prevalent--square pulses in conjunction with a low data rate suggest that a large number of particles are present in the probe volume. A maximum theoretical data rate of 100 kHz has been approximated by Spectron by using Restrictions 1 and 3 outlined previously.

TABLE 2. LIST OF INTENSITY RATIO BIN MAXIMUMS,
MINIMUMS, AND CENTERS FOR EACH BIN.

BIN RATIO RANGES				
BIN	WIDTH	MAXIMUM	MINIMUM	BIN CENTER
33	.1078e-01	0.30505	0.29427	0.29961
34	.1040e-01	0.29427	0.28387	0.28903
35	.1003e-01	0.28387	0.27384	0.27881
36	.9677e-02	0.27384	0.26416	0.26896
37	.9335e-02	0.26416	0.25483	0.25946
38	.9005e-02	0.25483	0.24582	0.25029
39	.8687e-02	0.24582	0.23714	0.24144
40	.8380e-02	0.23714	0.22876	0.23291
41	.8084e-02	0.22876	0.22067	0.22468
42	.7798e-02	0.22067	0.21288	0.21674
43	.7523e-02	0.21288	0.20535	0.20908
44	.7257e-02	0.20535	0.19810	0.20169
45	.7000e-02	0.19810	0.19110	0.19456
46	.6753e-02	0.19110	0.18434	0.18769
47	.6514e-02	0.18434	0.17783	0.18106
48	.6284e-02	0.17783	0.17154	0.17466
49	.6062e-02	0.17154	0.16548	0.16849
50	.5848e-02	0.16548	0.15963	0.16253
51	.5641e-02	0.15963	0.15399	0.15679
52	.5442e-02	0.15399	0.14855	0.15125
53	.5250e-02	0.14855	0.14330	0.14590
54	.5064e-02	0.14330	0.13824	0.14075
54	.4885e-02	0.13824	0.13335	0.13577
56	.4712e-02	0.13335	0.12864	0.13097
57	.4546e-02	0.12864	0.12409	0.12635
58	.4385e-02	0.12409	0.11971	0.12188
59	.4230e-02	0.11971	0.11548	0.11757
60	.4081e-02	0.11548	0.11140	0.11342
61	.3937e-02	0.11140	0.10746	0.10941
62	.3797e-02	0.10746	0.10366	0.10554
63	.3663e-02	0.10366	0.10000	0.10182



GRAPH OF NORMALIZED RAW COUNTS VERSUS
LOGARITHMIC INTENSITY RATIO FROM 1.0 TO 0.1

Date: 04/08/1985-1550
Series: 0.364MCAL Run: 0.460M-1B
Comment: HVA/HVB=1272/1520, L=20A, P=30PSI

MAX RAW COUNT = 30
TOTAL RAW COUNT = 630
SAMPLE TIME: .2 SECONDS

TOTAL REDUCED COUNT=166972
LINEAR MEAN DIA: .46 MICRONS
SURFACE MEAN DIA: .46 MICRONS
VOLUME MEAN DIA: .46 MICRONS
SAUTER MEAN DIA: .46 MICRONS
STANDARD DEVIATION: .46 MICRONS
SAMPLE TIME: .2 SECONDS

LISTING OF RAW COUNTS

RATIO	SIZE IN MICRONS	BIN COUNT	RATIO	SIZE IN MICRONS	BIN COUNT
.615	.3	5	.25	.44	22
.552	.32	6	.241	.45	14
.478	.34	7	.232	.45	30
.461	.34	5	.224	.45	24
.429	.35	6	.216	.45	19
.414	.35	8	.209	.45	19
.399	.36	10	.201	.45	30
.385	.38	12	.194	.45	18
.371	.4	11	.187	.46	19
.358	.41	15	.181	.46	11
.345	.42	18	.174	.46	29
.333	.42	22	.168	.45	15
.321	.43	11	.162	.46	15
.31	.43	29	.156	.46	13
.299	.43	16	.151	.46	6
.289	.43	21	.14	.46	8
.278	.44	29	.13	.42	11
.268	.44	21	.126	.41	5
.259	.44	22			

LISTING OF REDUCED COUNT RATE

SIZE IN MICRONS	RDUCD COUNT	BIN WIDTH	SIZE IN MICRONS	RDUCD COUNT	BIN WIDTH
.3	5	7E-03	.44	22	2E-03
.32	6	5E-03	.45	14	1E-03
.34	7	4E-03	.45	30	1E-03
.34	5	4E-03	.45	24	1E-03
.35	6	5E-03	.45	19	1E-03
.35	8	5E-03	.45	19	1E-03
.36	10	.01	.45	30	1E-03
.38	12	.019	.45	18	1E-03
.4	11	.017	.46	19	1E-03
.41	15	8E-03	.46	11	1E-03
.42	18	6E-03	.46	29	1E-03
.42	22	3E-03	.46	15	1E-03
.43	11	3E-03	.46	15	1E-03
.43	29	3E-03	.46	13	1E-03
.43	16	2E-03	.46	6	1E-03
.43	21	2E-03	.46	8	-.018
.44	29	1E-03	.42	11	-.016
.44	21	2E-03	.41	5	-1E-03
.44	22	2E-03			

Figure 10. Sample Output of the IPSS

D. CALIBRATION PARTICLES

The scatterers used for system calibration, theoretical analysis, and performance determination were polystyrene latex spheres of known size obtained from Duke Scientific Corporation of Palo Alto, California and Seragen Diagnostics (formerly Dow Chemical Company) of Indianapolis, Indiana. These particles, suspended in an admixture of water and surfactant, are listed in Table 3. Both companies report the density as 1.05 g/mL and the refractive index as 1.59 at 589.26 nm. Spectron reports a refractive index of 1.57 at 488.0 nm. All particle solutions from Duke Scientific are 0.5 percent solid by weight, except the 0.412 μm size which is 10 percent solid by weight. All of the Dow solutions are 10 percent solid by weight. Samples are prepared by withdrawing solution from the highly concentrated solution with a microliter syringe and diluting them with 200 ml deionized water or methanol. Particles in this resulting solution are then atomized by a TSI Constant Output Atomizer.

E. PARTICLE GENERATION SYSTEM

The TSI Constant Output Atomizer (Model 3076) is shown in Figure 11. Compressed air is first dried and filtered before being supplied to the atomizer assembly. In the assembly, the air is expanded through a small hole (0.0135 inches) to form a high-velocity jet. The solution is drawn by the jet to the atomizer where large droplets are removed by impaction on the wall of the atomizer. The excess liquid returns to the container. The aerosol travels to the diffusion drier (TSI Model 3062) shown in Figure 12. The dried aerosols are injected through a nozzle centered above the optical probe volume.

F. CALIBRATION AND APPLICATION OF THE IPSS

The Mie theory (References 1, 3, and 4) shows that the scattered intensity ratio at angles of scatter, θ and ϕ , can be found if the refractive indices of both the particle and surrounding medium, the wavelength and polarization of the incident radiation, and the diameter of the scatterer are all known. However, in experimental applications (soot-sizing measurements), the IPSS

TABLE 3. PARTICLE SIZES AVAILABLE FOR EXPERIMENTATION.

MEAN DIAMETER (μm)	STANDARD DEVIATION (μm)
0.087*	0.0046 (5.3%)
0.109*	0.0027 (2.5%)
0.173	0.0068 (3.9%)
0.198	0.0036 (1.8%)
0.215	0.0026 (1.2%)
0.255*	0.0022 (0.9%)
0.261	0.0031 (1.2%)
0.272	0.0031
0.312	0.0022 (0.7%)
0.330	0.0040
0.364*	0.0024 (0.7%)
0.412	0.0058 (1.4%)
0.460	0.0048 (1.0%)
0.497	0.0059 (1.2%)
0.500*	0.0027 (0.5%)
0.605	0.0089 (1.5%)
0.624*	0.0052 (0.8%)
0.760	0.0046
0.804*	0.0048 (0.6%)

* Obtained from Duke Scientific Corporation

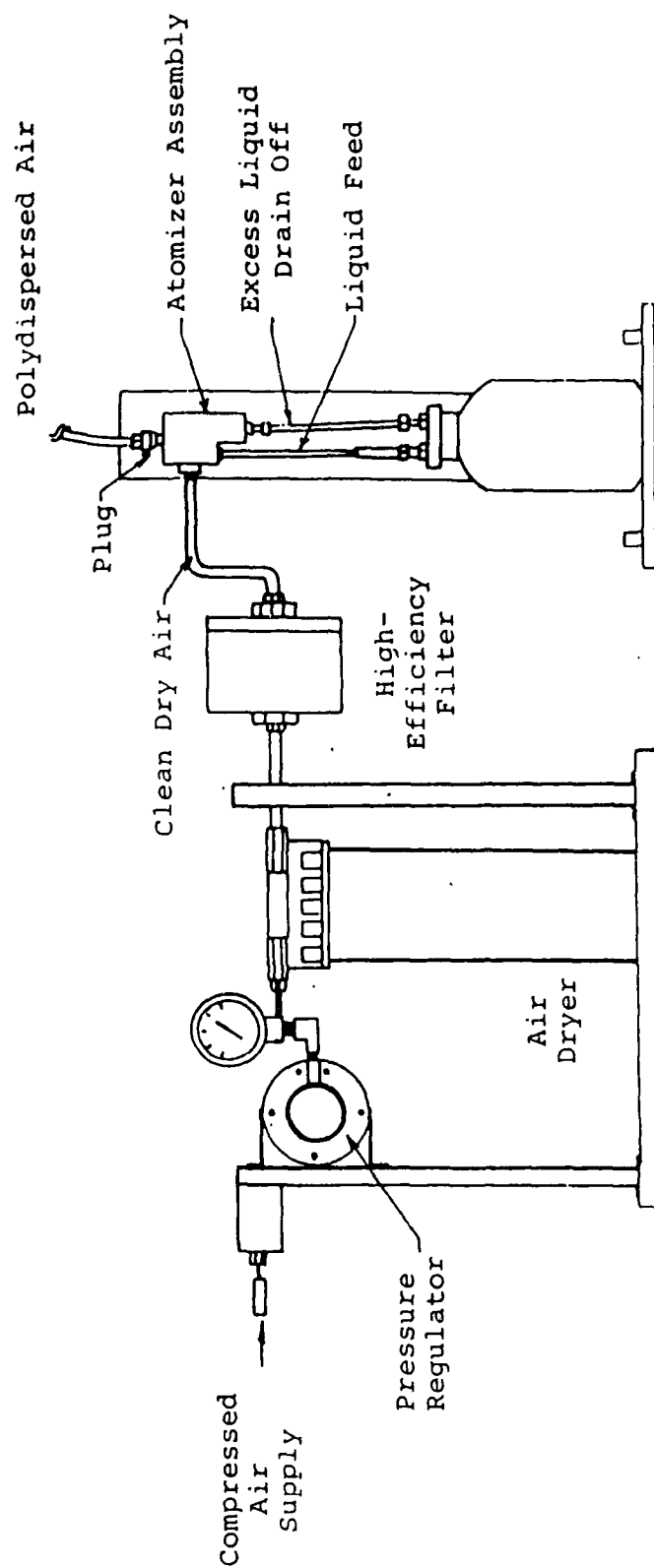


Figure 11. TSI Constant Output Atomizer

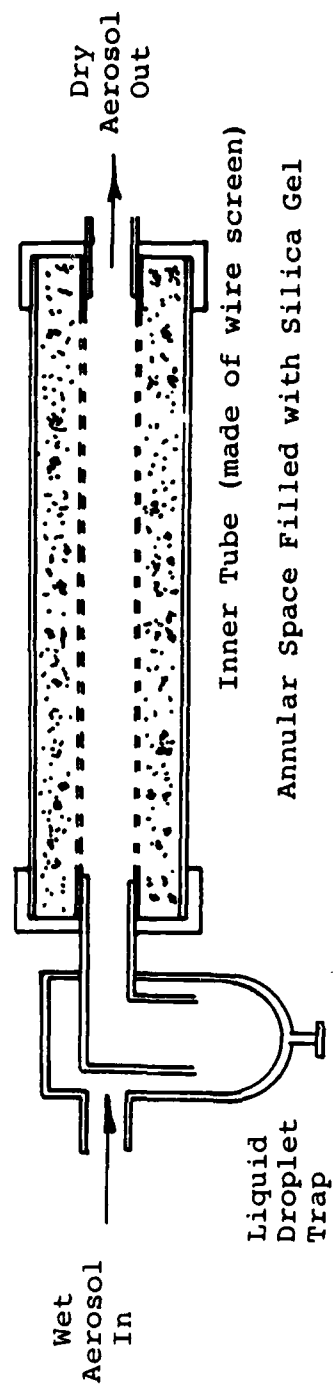


Figure 12. Diffusion Drier

requires the solution of the inverse problem--that is, the scattered intensity ratio is known (through measurement) and the particle size must be determined. As stated earlier, this correlation is provided by the bin tables present in the IPSS software package. However, to ensure that the IPSS correctly reports the diameter, the system must first be calibrated by injecting latex particles of known size and adjusting the PMT gains until the measured mean diameter matches the size of the injected particles.

Previously, the standard procedure for delivering the particles to the probe volume for calibration was to dilute them in deionized water and pass the resulting suspension through an atomizer to form droplets. The droplets, then, are mixed with dry air, exposing the particles in their natural size and refractive index in the probe volume. It was discovered that droplets of water escaping from the particle-drying system were overwhelming the signals from the control volume. This resulted in size measurement bias towards a static distribution; the system could not respond to different size particles. Dilution with a more volatile noninterfering liquid, such as methanol allows the system to respond effectively to different size particles. The size distributions obtained were narrower; the repeatability of the results was found to be more consistent, and the measured mean diameter for each particle approached the nominal diameter specified by the manufacturer. Because alcohols can disturb the size of the latex particles with time, a new particle solution should be used for every calibration of the instrument. Figure 13 displays the measured linear mean diameter versus the corresponding nominal diameter of each particle measured.

During calibration, a particle solution was diluted to half the original concentration to check the type of scattering occurring at the probe volume. Correspondingly, the data rate decreased by almost half. The above seems to indicate that single scattering is the most important scattering process occurring at the probe volume. Figures 14a, and 14b show normalized size distribution histograms for 0.412 μm latex particle solutions of arbitrary concentrations c_1 and one-half of c_1 , respectively.

Also during calibration of the 40°/20° angle pair, some of the diameter bin widths listed in the IPSS data output table (and used in the calculation

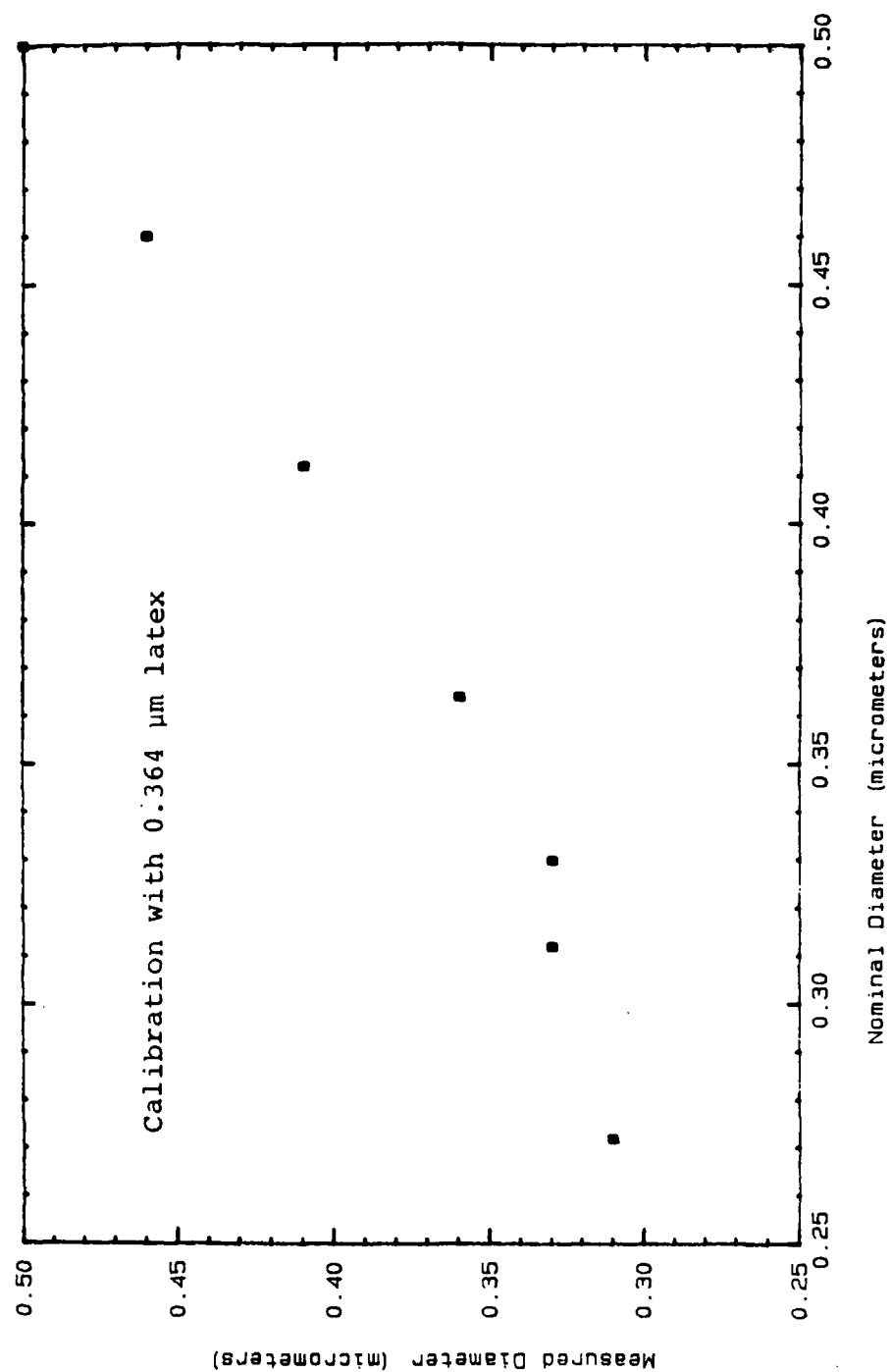
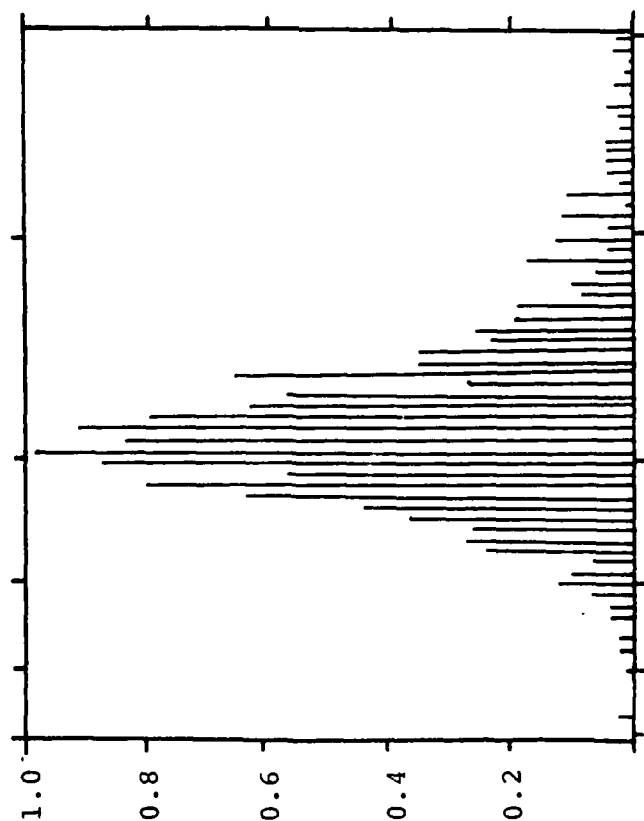


Figure 13. Measured Linear Mean Diameter versus Nominal Diameter of Latex Spheres.

Date: 07/01/85
 Series: 0.412MCAL Run: 0.412M-01
 Comment: D=0.412M HV=1070/1370 LASER=20A

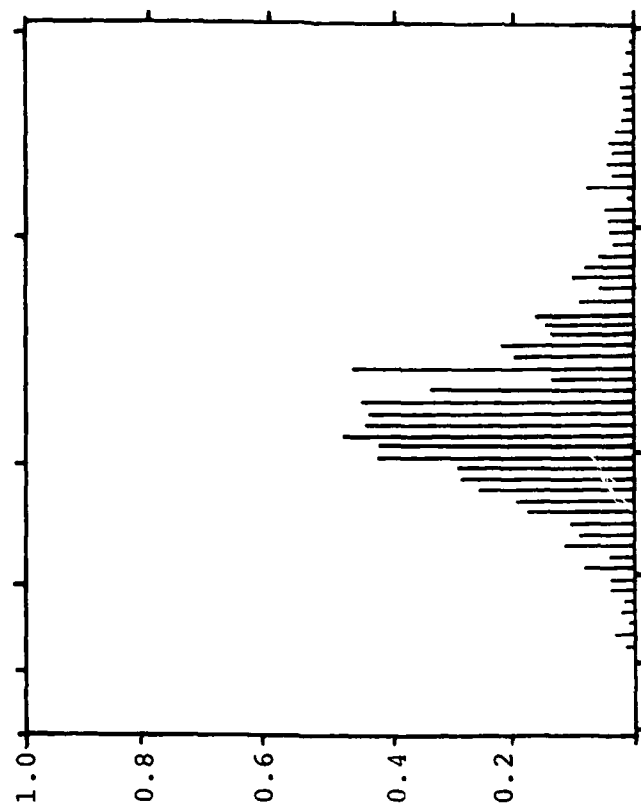
MAX RAW COUNT = 152
 TOTAL RAW COUNT = 2123
 SAMPLE TIME: 33.9 SECONDS



(a)

Date: 07/01/85
 Series: 0.412MCAL Run: 0.412M-02
 Comment: D=0.412M HV=1070/1370 LASER=20A

MAX RAW COUNT = 152
 TOTAL RAW COUNT = 2373
 SAMPLE TIME: 69.8 SECONDS



(b)

Figure 14. Normalized Graph of Raw Counts versus Size

of the standard deviation) were found to have negative bin widths. A comparison of the theoretical values (obtained from the Mie code found in Reference 4) with the IPSS bin table data (intensity ratio bin centers versus diameter bin centers for the angle pair $40^\circ/20^\circ$ and refractive index of latex, 1.57-10.0), shown in Figure 15, revealed a disagreement between the two plots. This disagreement was unexpected since it appears that the IPSS bin tables were produced by an interpolation of intensity ratios obtained from Mie code output. The discrepancy is currently attributed to the assumption of constant absolute scattered intensity within the solid angle of each collection lens. The theoretical plots shown in the following discussion were obtained from this assumption and are not expected to be valid for the solid angle present in the IPSS. Through interfacing the Mie code with algorithms which will generate data points on the lens and integrate these points over the solid angle of the receiving lens, the theoretical plot is expected to collapse to the plot provided by the IPSS bin tables.

Although the theoretical plots do not agree with IPSS bin table plots, the trends are correct. Hence, the presence of negative bin widths can be explained. In addition, insight is gained into the sensitivity and performance of the instrument. In a closer examination of the theoretical intensity ratio curve at a refractive index of 1.57 and an angle pair of $40^\circ/20^\circ$, a local minimum and maximum between the diametric range of $0.53\text{ }\mu\text{m}$ and $0.60\text{ }\mu\text{m}$ is found (Figure 16). Thus, in this small region, the intensity ratio is multivalued. If such a behavior is not considered when developing and implementing an interpolation scheme to generate bin table data, results such as negative bin widths can be obtained. The bending of the curve back onto itself in the bin plot table, shown in Figure 15, demonstrates the negative bin widths resulting from the presence of a local maximum and minimum. Since particle size cannot be resolved in these multivalued regions, calibration in or near these areas must be avoided.

Similar comparisons for the other angle pairs of both the large and small-angle ratioing technique can also be made. As shown in Figures 17 and 18, the scattered intensity ratio versus diameter curves for latex at the other angle pairs of the large-angle ratioing technique ($50^\circ/20^\circ$ and $60^\circ/20^\circ$) do not exhibit multiplicities in the range of measurement specified by Spectron. It

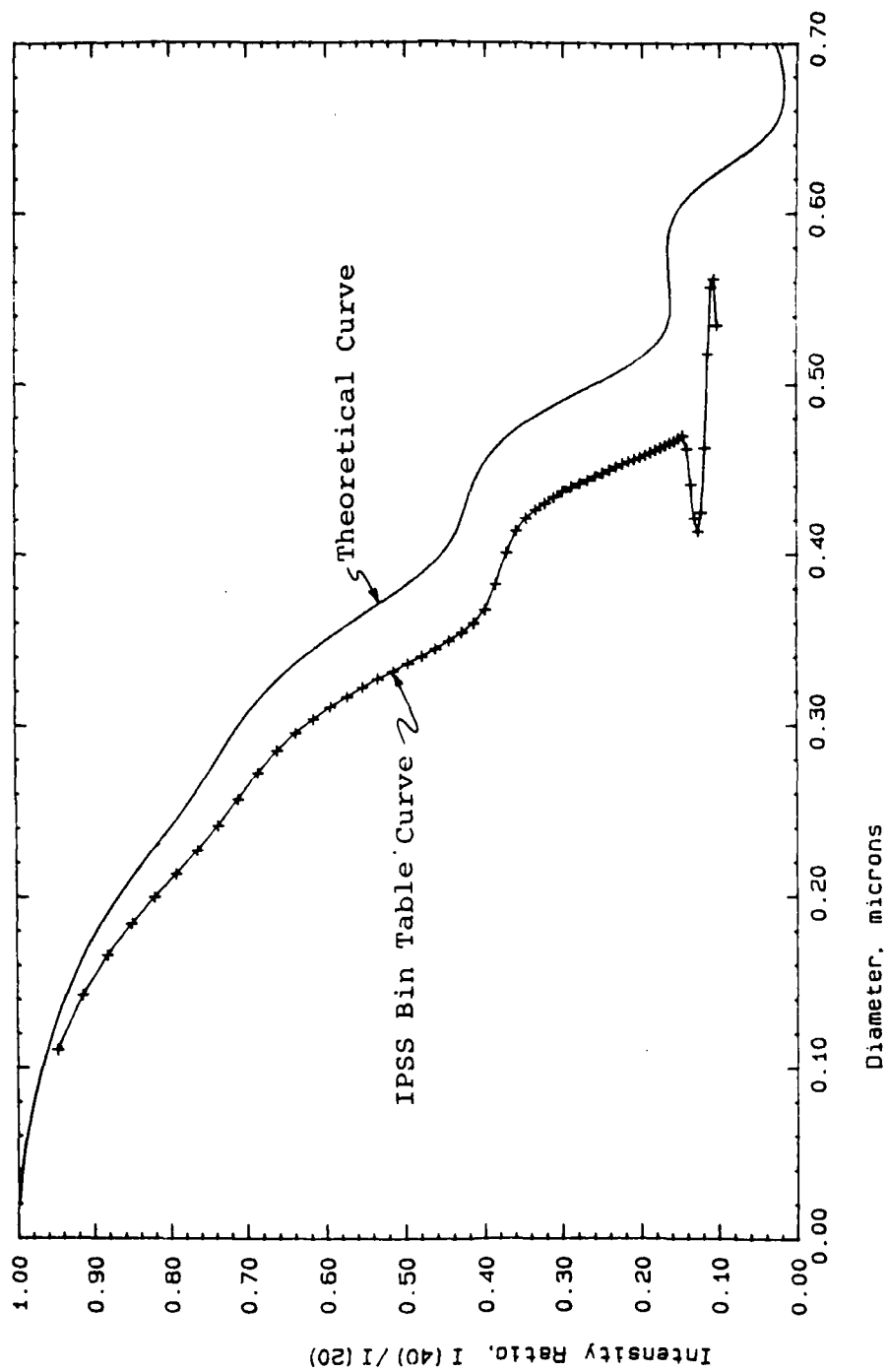


Figure 15. Comparison of Theoretical Intensity Ratio versus Diameter with the IPSS Bin Center Tables for a $40^\circ/20^\circ$ Angle Pair and a Real Refractive Index of 1.57.

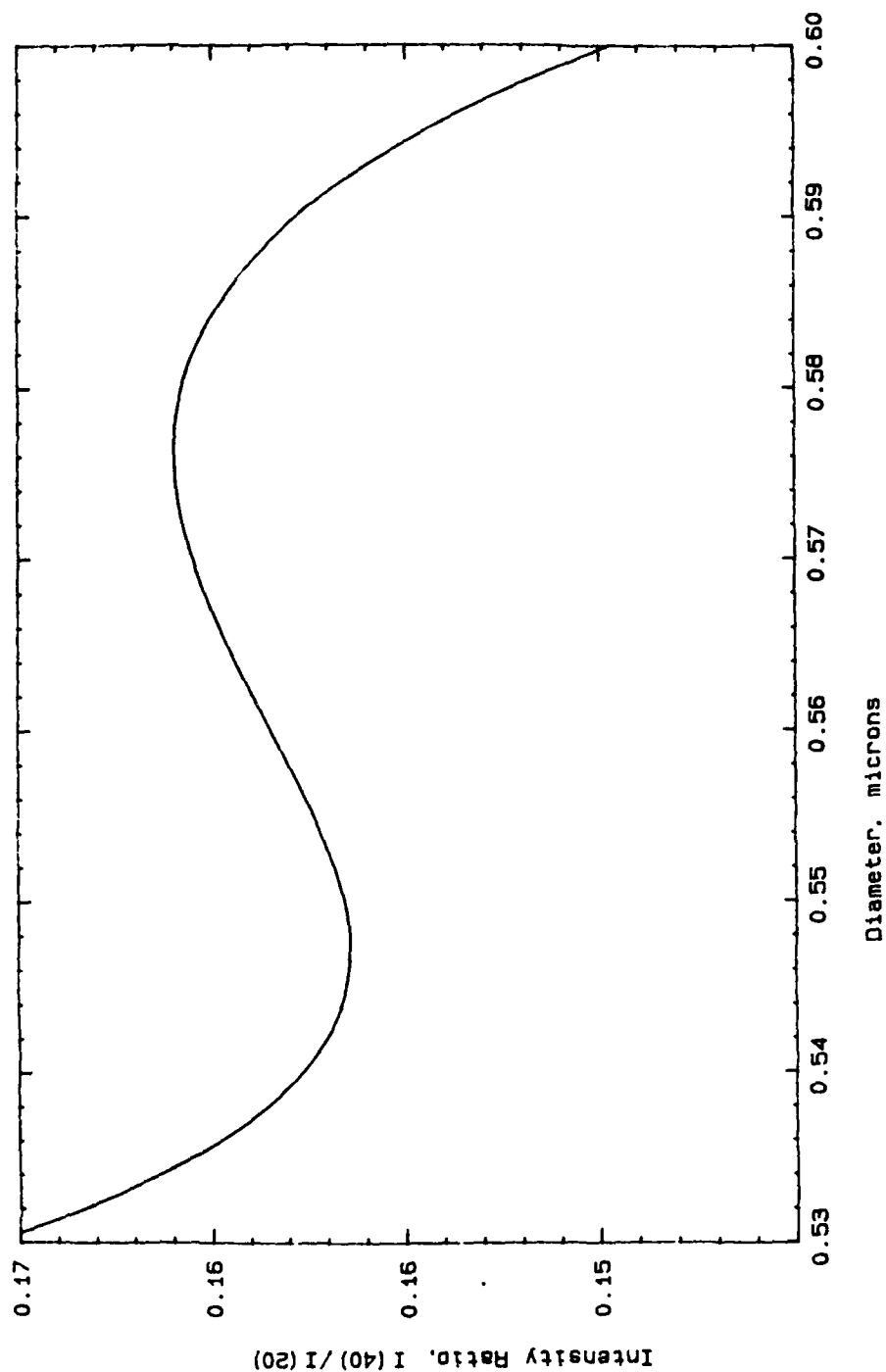


Figure 16. A Closer Examination of the $40^\circ/20^\circ$ Angle Pair for a Real Refractive Index of 1.57 and the Diametric Range of 0.53 μm to 0.60 μm .

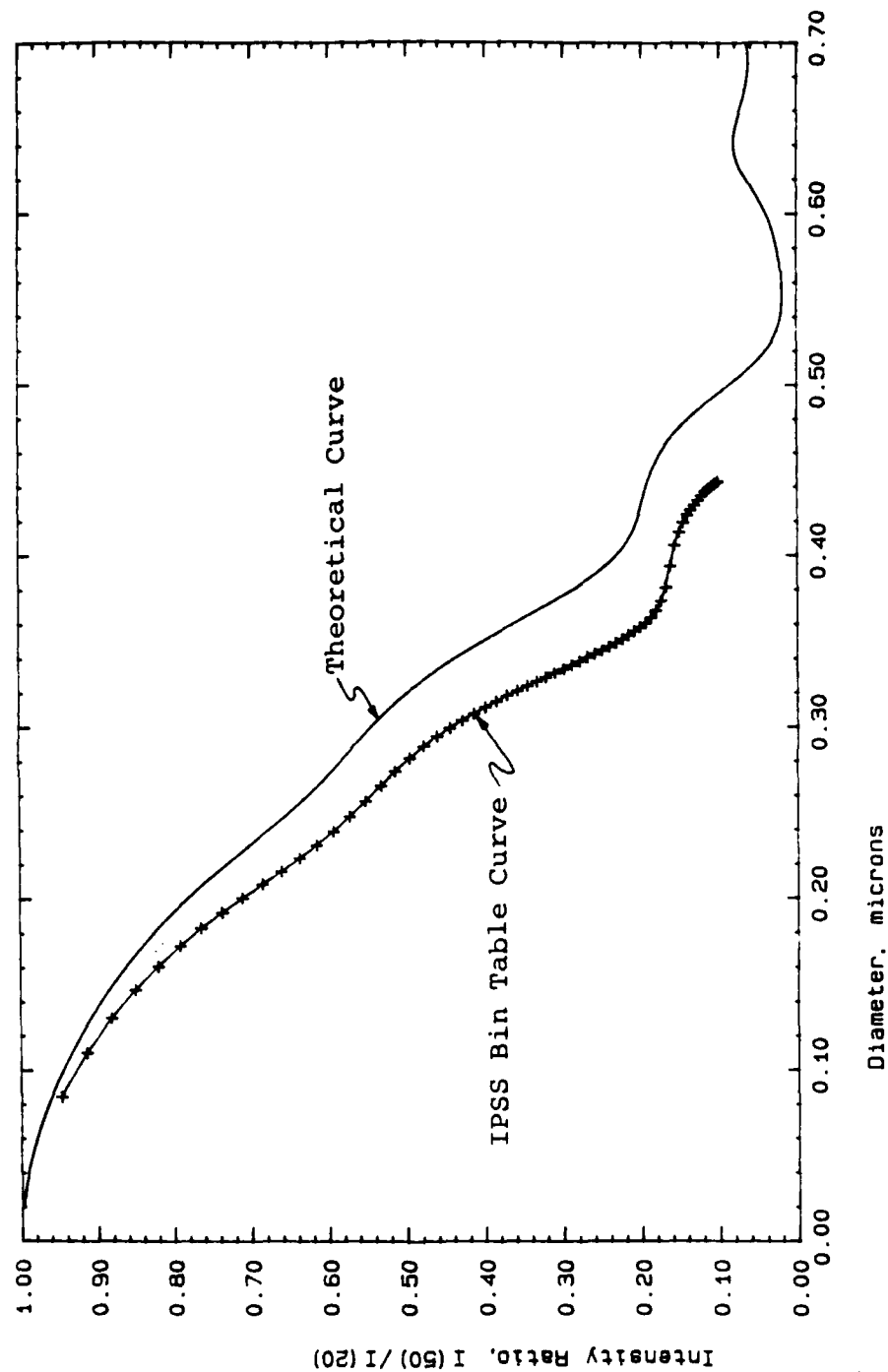


Figure 17. Comparison of Theoretical Intensity Ratio versus Diameter with the IPSS Bin Center Tables for a 50°/20° Angle Pair and a Real Refractive Index of 1.57.

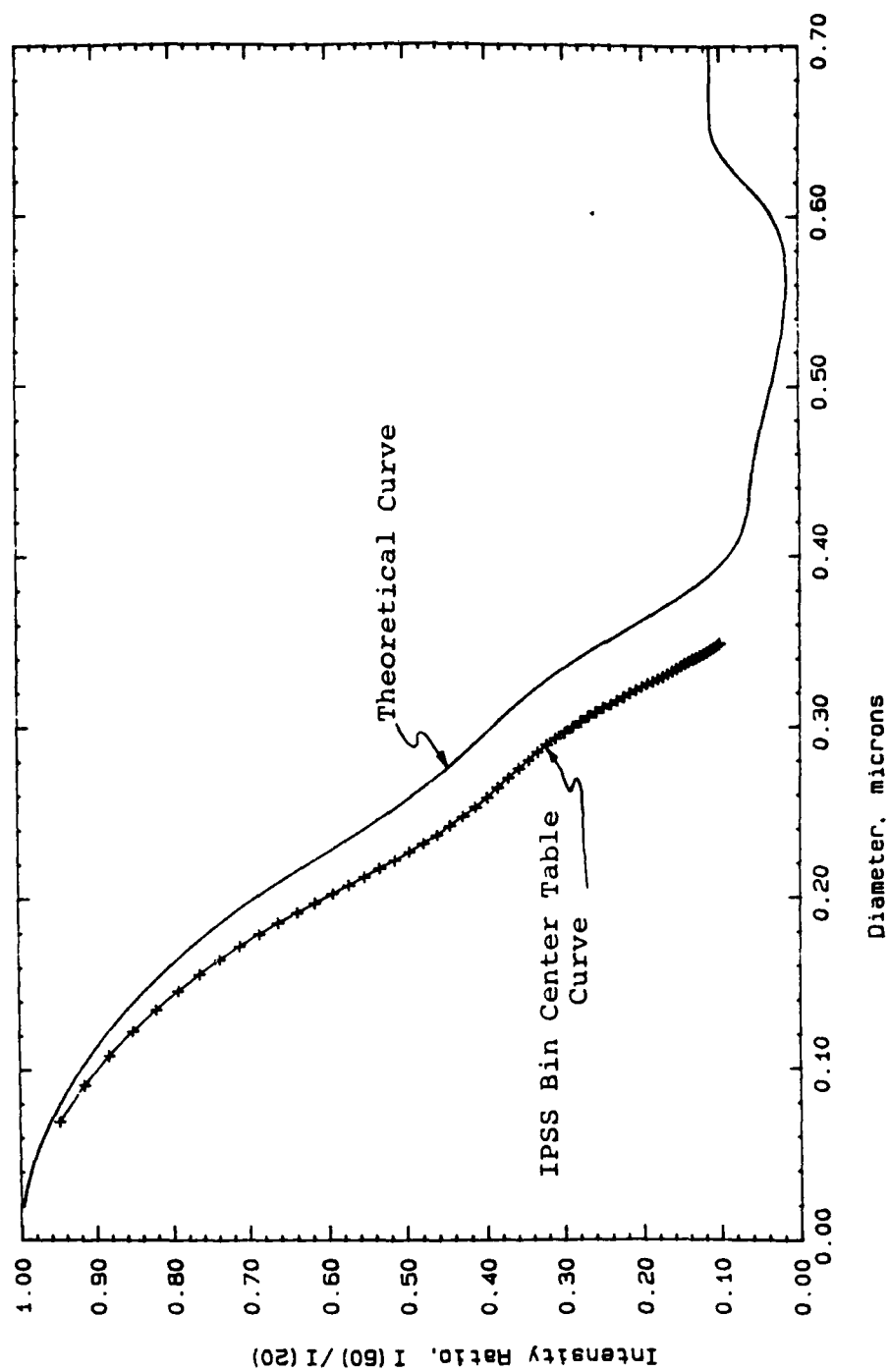


Figure 18. Comparison of Theoretical Intensity Ratio versus Diameter with the IPSS Bin Center Tables for a $60^\circ/20^\circ$ Angle Pair and a Real Refractive Index of 1.57.

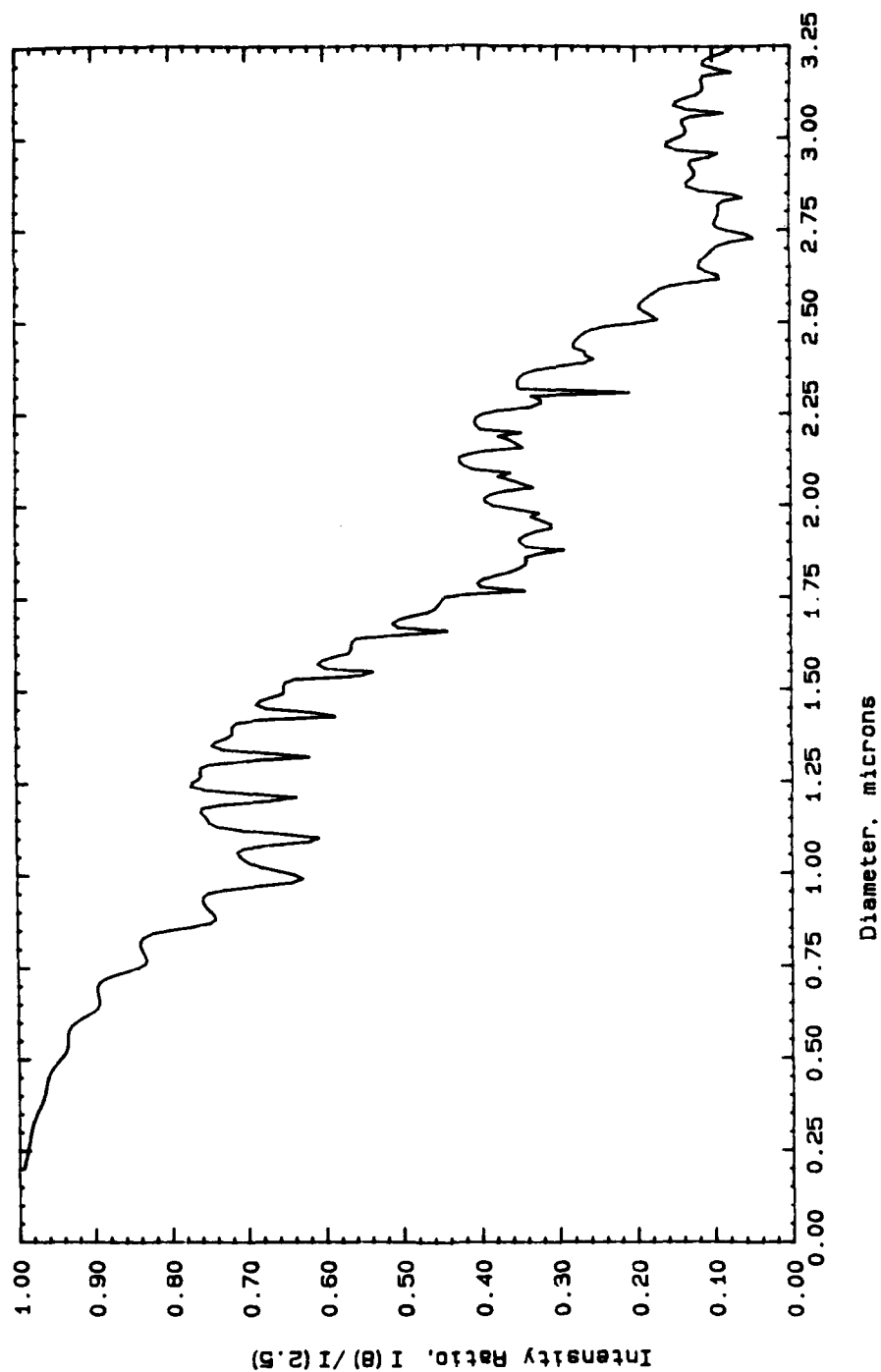


Figure 19. Plot of Intensity Ratio versus Diameter for an $8^\circ/2.5^\circ$ Angle Pair and a Real Refractive Index of 1.57.

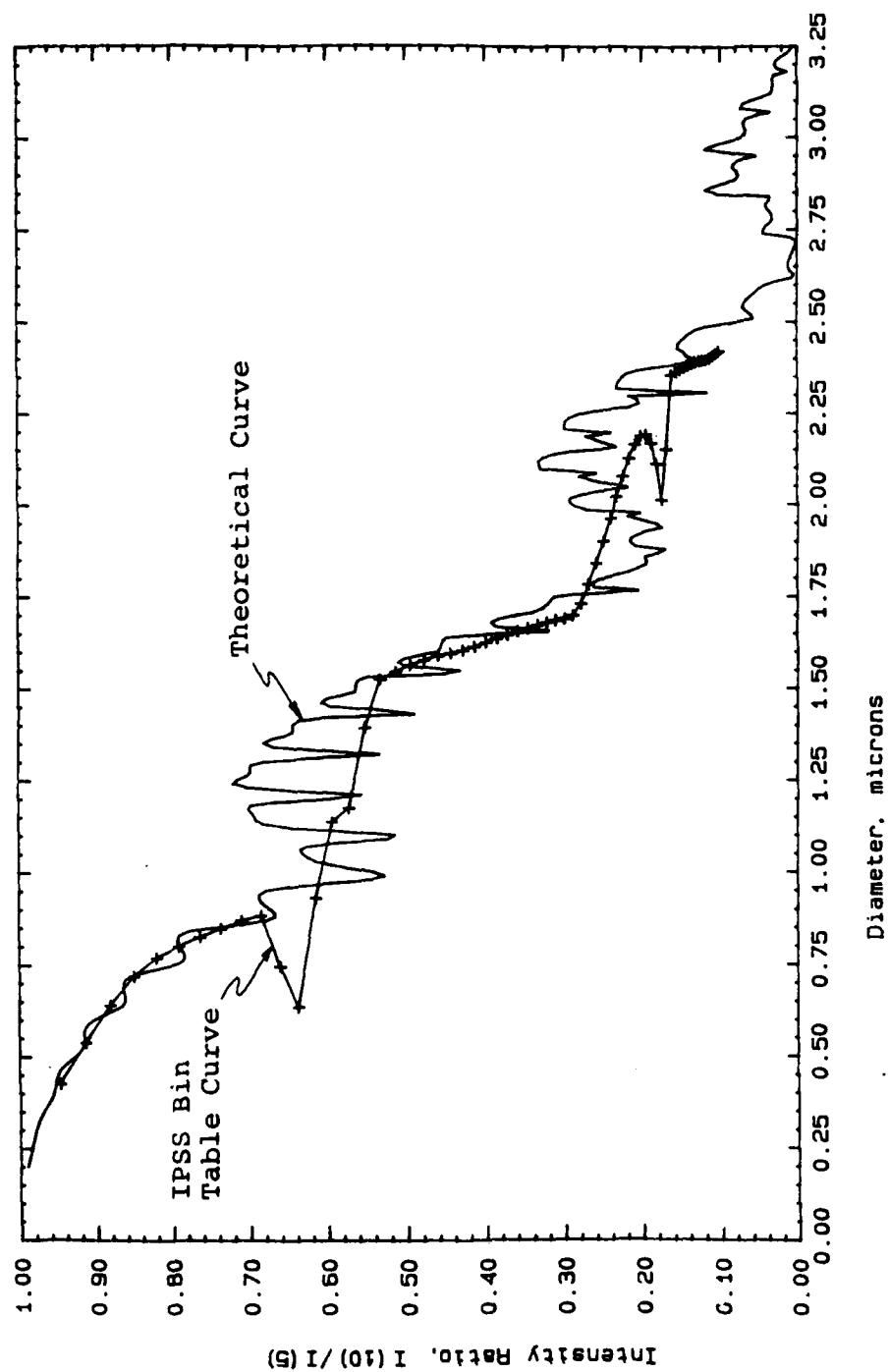


Figure 20. Comparison of Theoretical Intensity Ratio versus Diameter with the IPSS Bin Center Tables for a $10^\circ/5^\circ$ Angle Pair and a Real Refractive Index of 1.57.

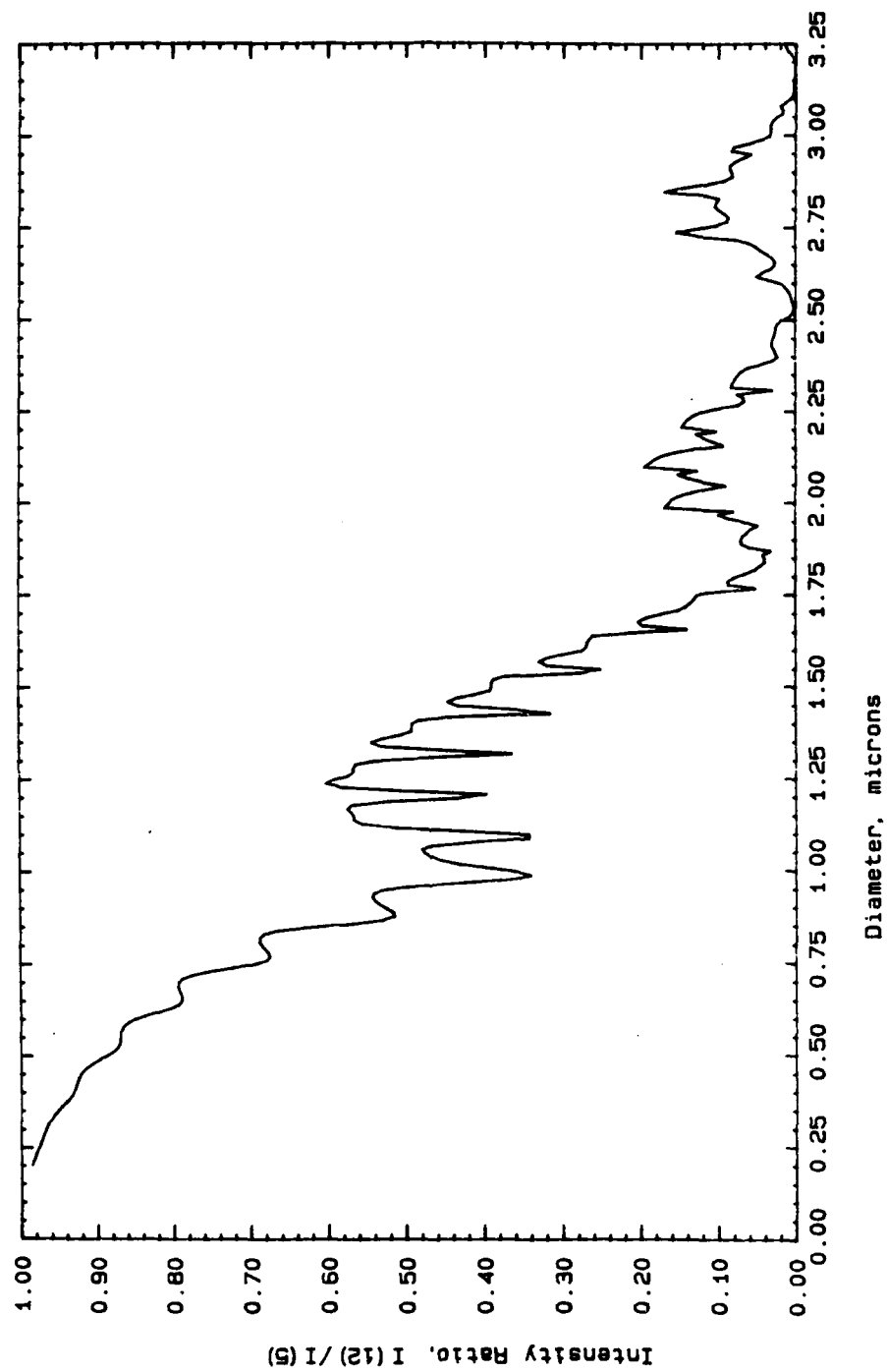


Figure 21. Plot of Intensity Ratio versus Diameter for a $12^\circ/5^\circ$ Angle Pair and a Real Refractive Index of 1.57.

is expected, then, that no difficulties should be encountered when implementing these angle pairs. Unfortunately, the same comments cannot be made about the small-angle ratioing technique for latex. For such small-angle pairs, the presence of a real refractive index is responsible for rapid oscillations in the intensity ratio versus diameter curves (Figures 19 through 21). Again, the local maximums and minimums are responsible for the calculations of negative bin widths. However, due to the presence of the numerous oscillations, the calculation of bin tables become difficult, if not impossible. The bin table plot for the $10^\circ/5^\circ$ angle pair (shown in Figure 20) and the absence of bin tables for the remaining angle pairs demonstrate this point. At its best, then, the small-angle ratioing technique for particles possessing a real refractive index is severely limited to extremely small size ranges outside the range of oscillations.

Finally, for the case of scatterers possessing a complex refractive index (Figures 22 through 27), the intensity ratio versus diameter curves are well-behaved for both small and large-angle ratioing techniques. However, since instrument calibrations are carried out with latex particles (having a real refractive index), the "goodness" of the measuring technique for soot (having a complex refractive index) is dependent on how well-behaved the latex curves are. Therefore, the use of the small-angle ratioing technique for soot size measurements does not look promising.

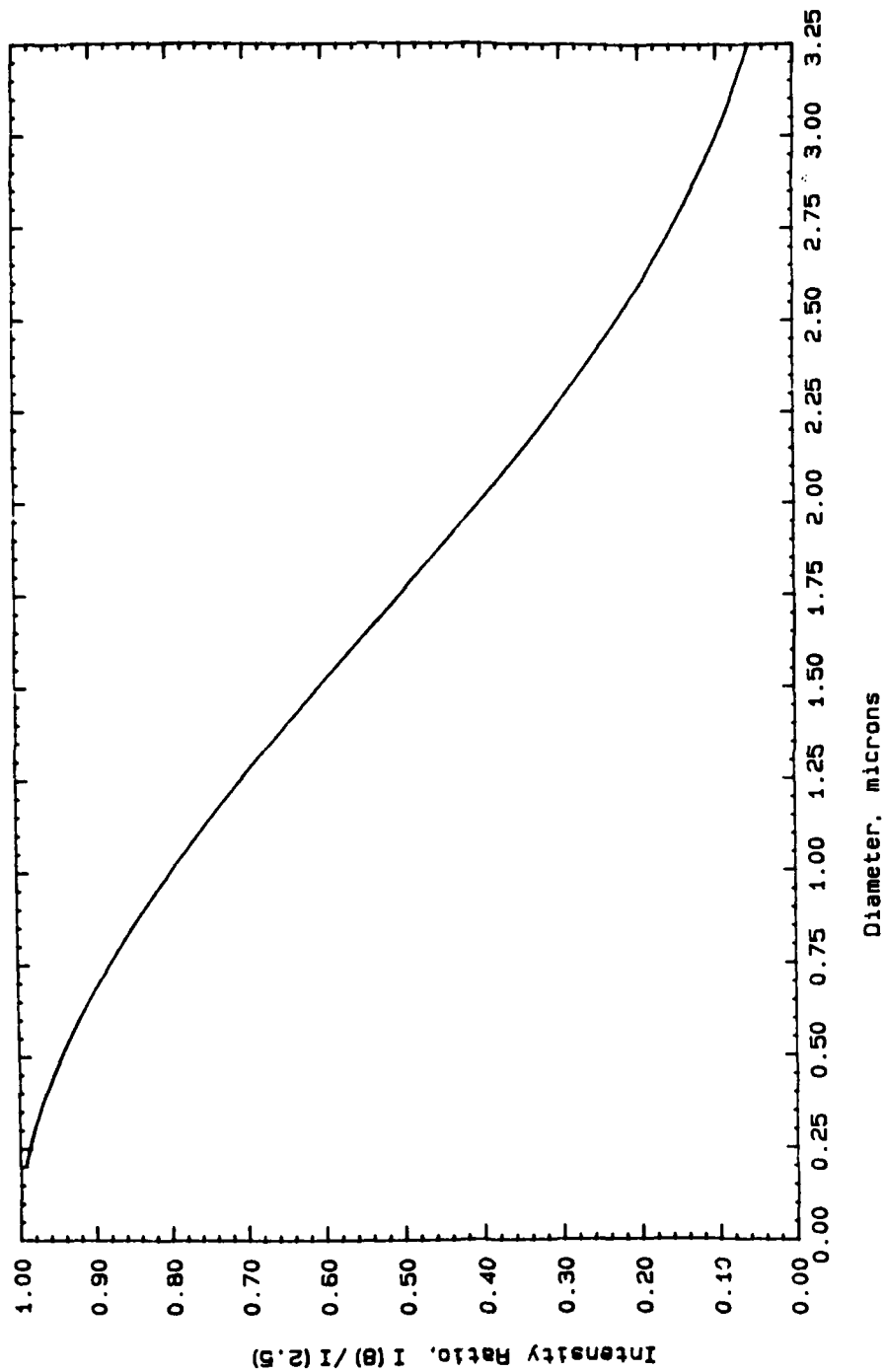


Figure 22. Plot of Theoretical Intensity Ratio versus Diameter for an $8^\circ/2.5^\circ$ Angle Pair and a Complex Refractive Index of $1.57 - i0.56$.

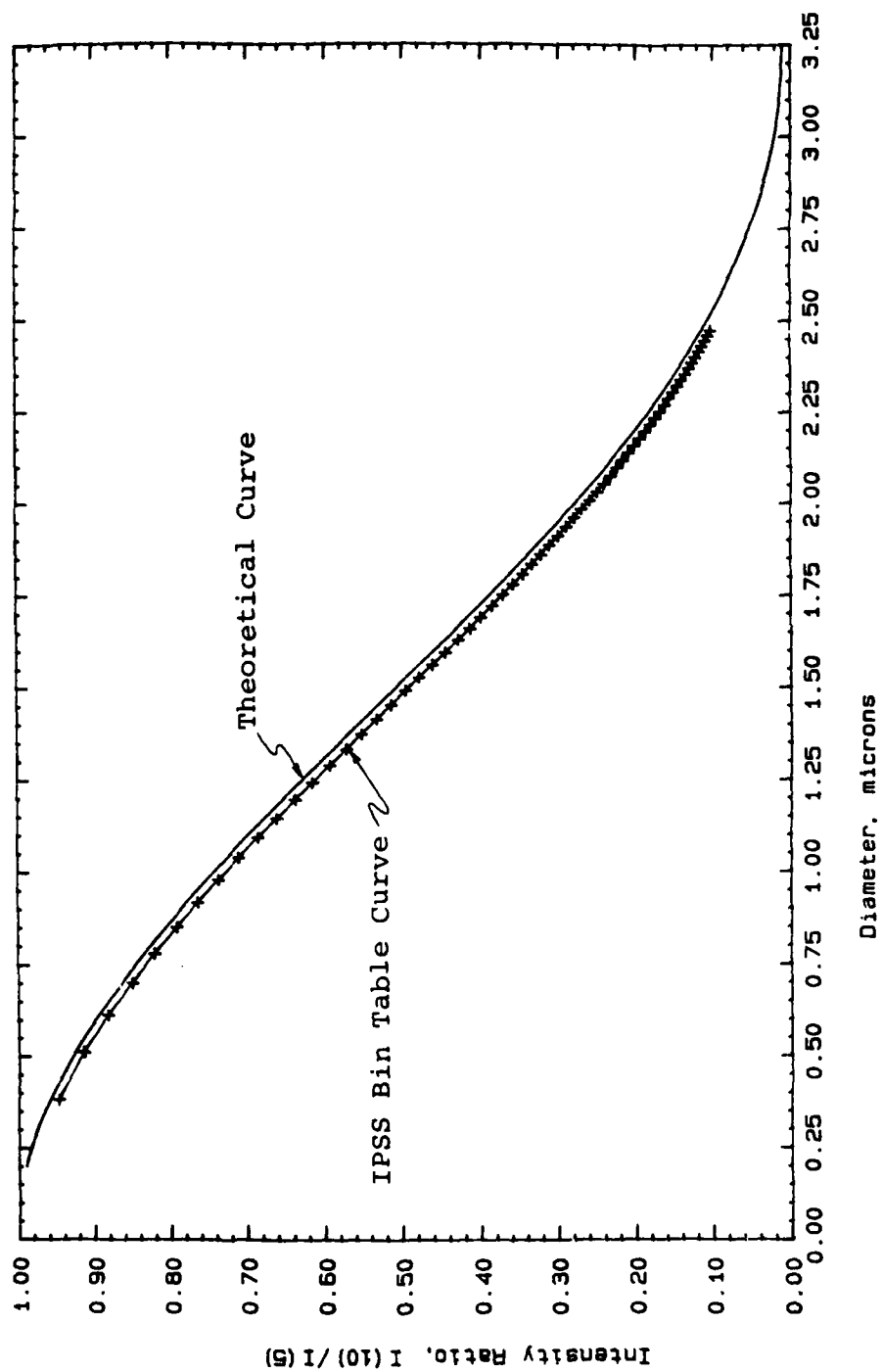


Figure 23. Comparison of Theoretical Intensity Ratio versus Diameter with the IPSS Bin Center Tables for a $10^\circ/5^\circ$ Angle Pair and a Complex Refractive Index of $1.57 - i0.56$.

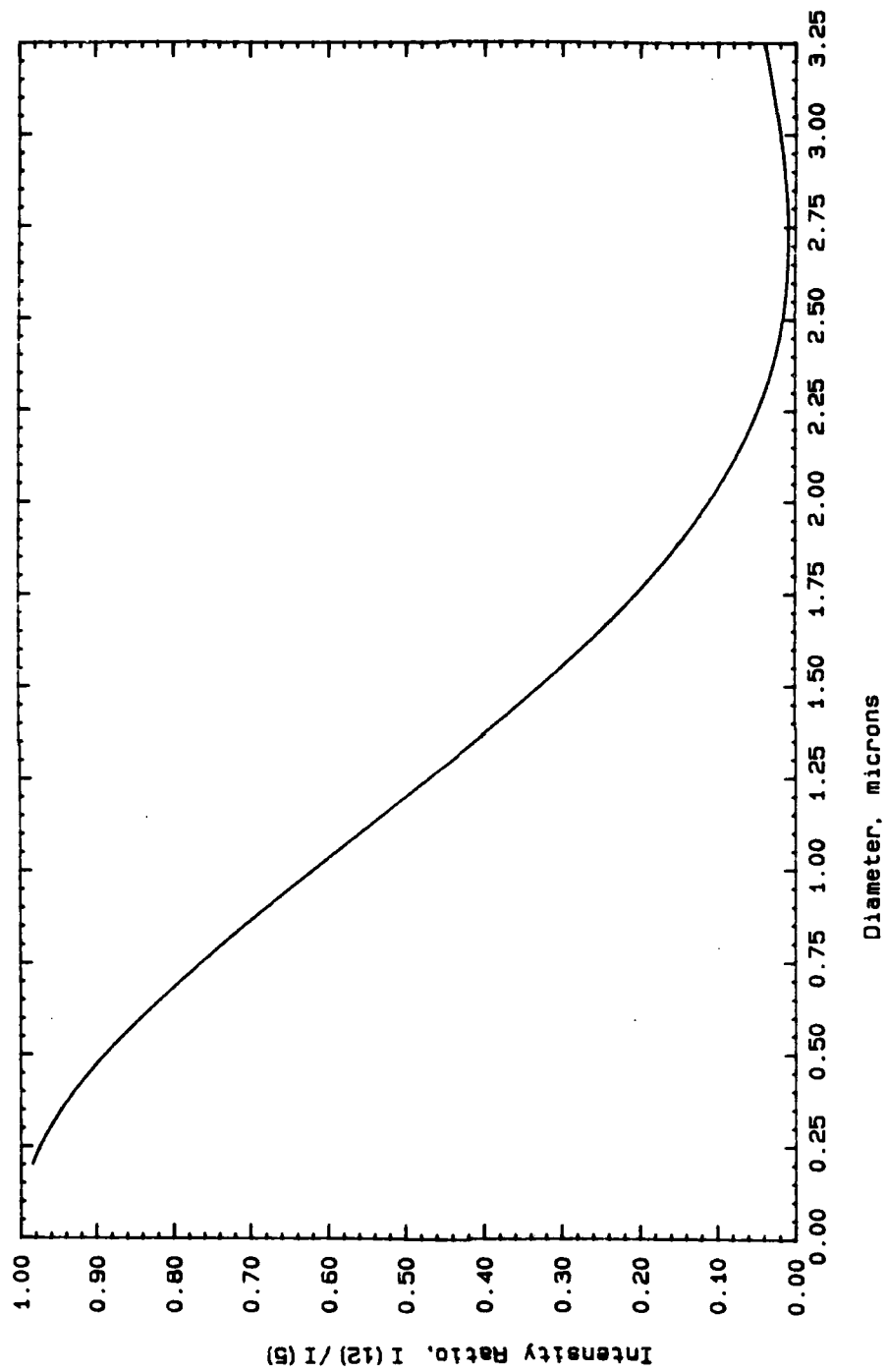


Figure 24. Plot of Theoretical Intensity Ratio versus Diameter for a $12^\circ/5^\circ$ Angle Pair and a Complex Refractive Index of $1.57 - i0.56$.

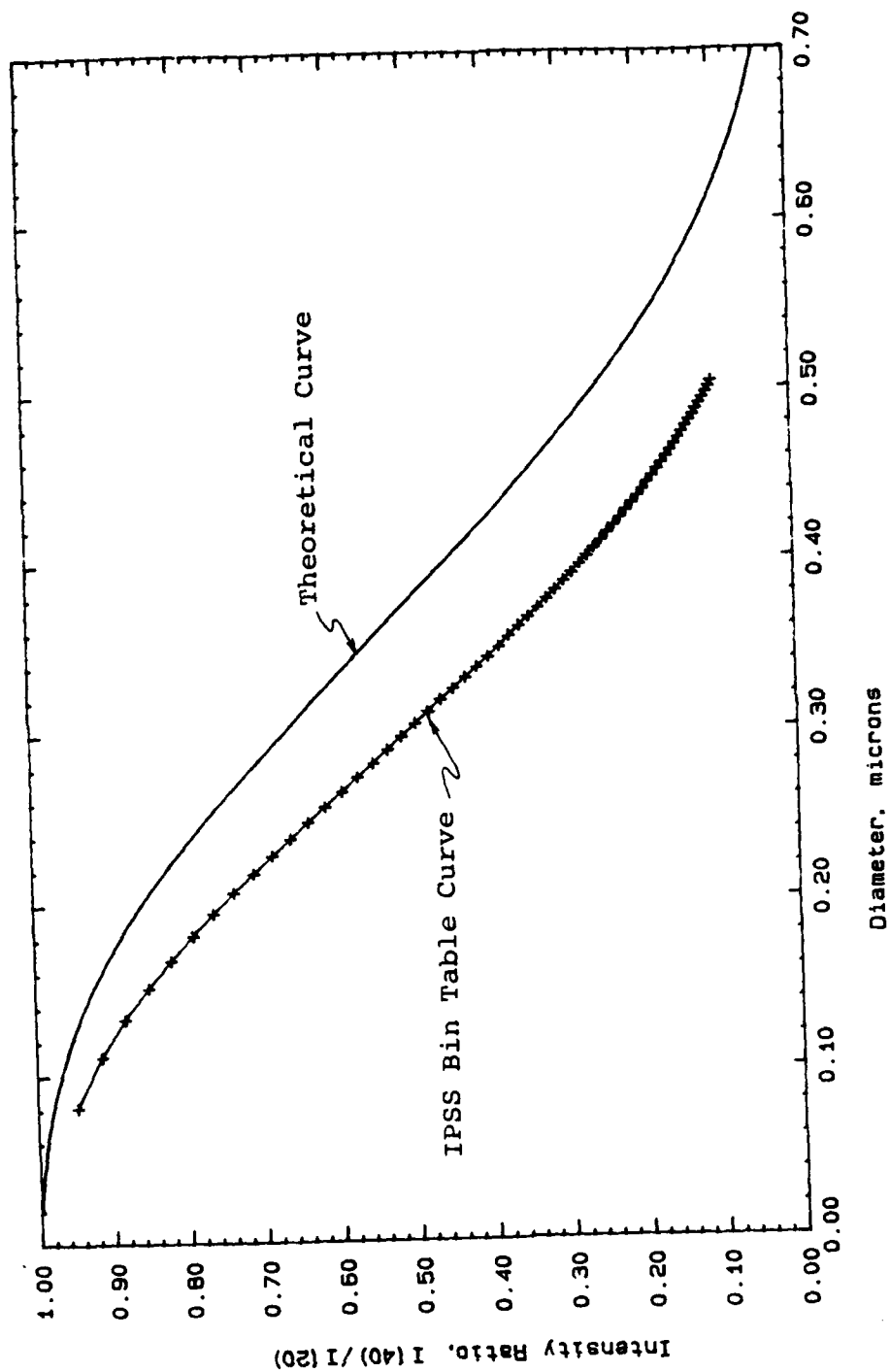


Figure 25. Comparison of Theoretical Intensity Ratio versus Diameter with the IPSS Bin Center Tables for a $40^\circ/20^\circ$ Angle Pair and a Complex Refractive Index of $1.57 - 0.56i$.

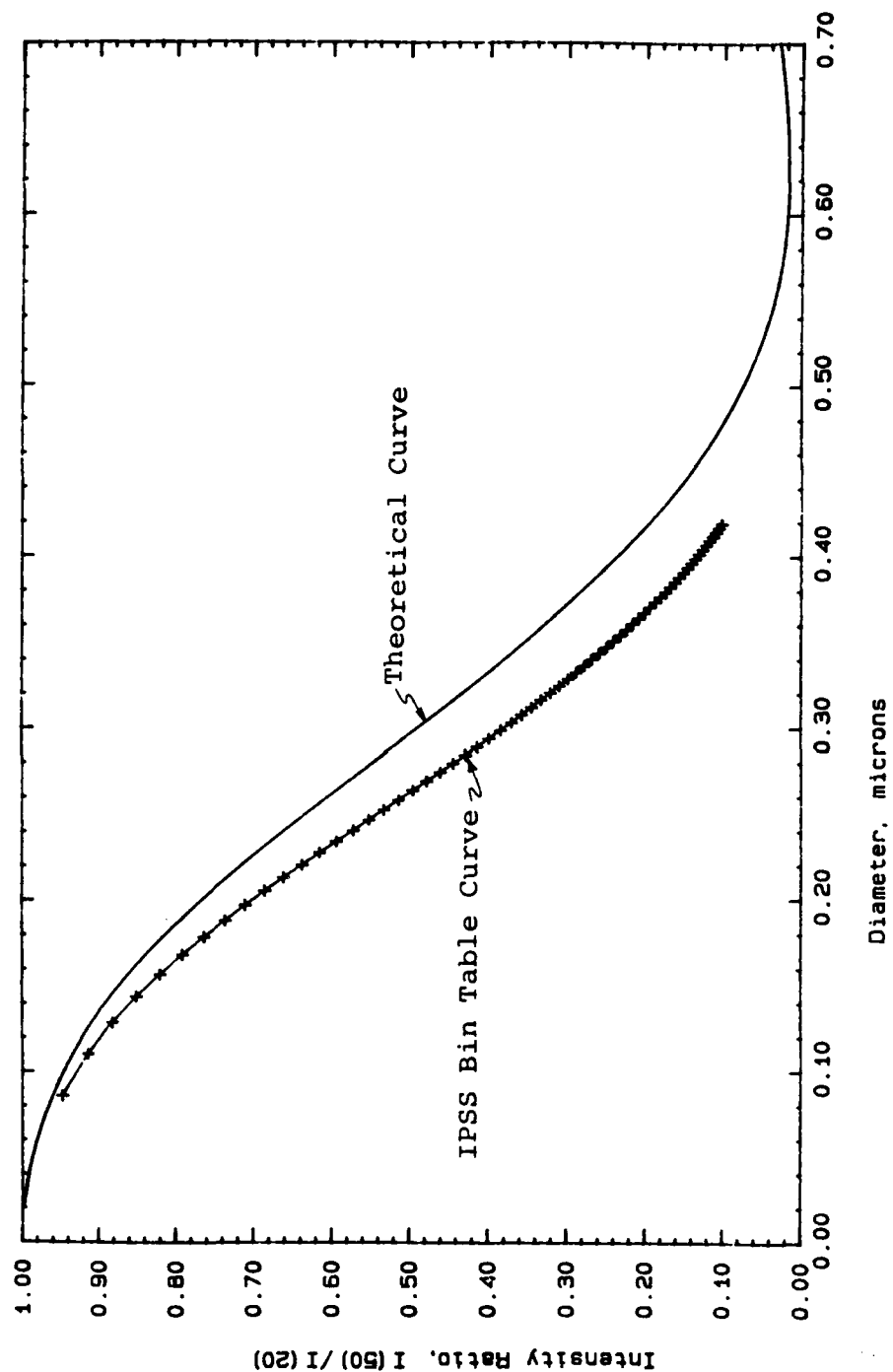


Figure 26. Comparison of Theoretical Intensity Ratio versus Diameter with the IPSS Bin Center Tables for a $50^\circ/20^\circ$ Angle Pair and a Complex Refractive Index of $1.57 - 0.56$.

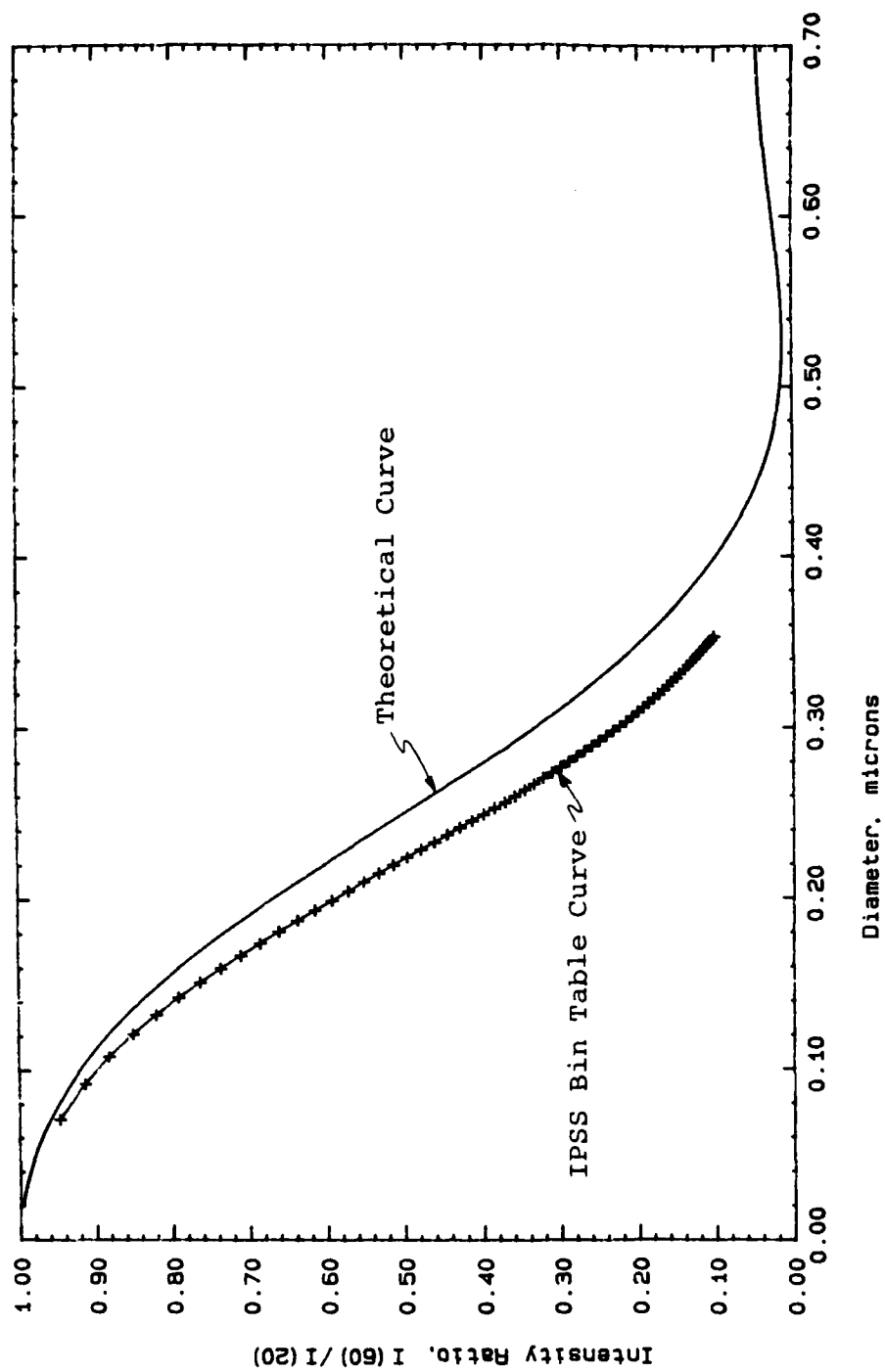


Figure 27. Comparison of Theoretical Intensity Ratio versus Diameter with the IPSS Bin Center Tables for a $60^\circ/20^\circ$ Angle Pair and a Complex Refractive Index of $1.57 - i0.56$.

SECTION IV

CONCLUSIONS AND RECOMMENDATIONS

It has been shown that the scattered intensity depends on the magnitude, wavelength and polarization of the incident intensity, the refractive indices of the particle and the medium outside the particle, the particle size and its geometry, the distance away from the center of the particle, and the angles of scatter. The assumptions made to arrive at the Mie expression are as follows:

1. both ϵ , μ , and σ are isotropic, time-independent electromagnetic properties,
2. the electric and magnetic fields are spatially and temporally continuous,
3. either the conductivity, σ , is zero or is included in the measurement of the imaginary part of the refractive index,
4. the scattering is restricted to single, elastic, and independent scattering,
5. the particle is spherical,
6. the particle material is homogeneous,
7. the magnetic permeability of the particle is equal to the magnetic permeability of the outside medium,
8. the relative refractive index--that is, the ratio of the refractive index of the particle to that of the outside medium--must be known.
9. no free surface charge is present on the particle,
10. the incident radiation is a time-harmonic, plane wave, and
11. the scattered radiation is measured far from the point of scatter so that the longitudinal electric field is negligible.

The IPSS design complies with the last two limitations by the placement of the detectors in the far field and the implementation of the laser as the incident source. The remaining limitations are imposed on the system by the shape and composition of the particle and are, therefore, possible sources of uncertainty in measurement. The effects of particles with varying refractive indices and aspherical shape on the accuracy of an instrument using a variation of the small-angle ratioing technique have been studied by Reference

8. Although the conclusions drawn in that study may not be valid for the large-angle pairs of the IPSS, the same experimental procedures can be used to test the IPSS's response to these effects. The effect of charged particles on the system is also a topic for further research since these particles are present during combustion. Reference 9 has presented the groundwork for the theoretical study of this problem.

In Section III, it was proposed that the theoretical plot would collapse to the IPSS bin table plots once integration over the solid angle was performed. Preliminary results have shown that this is not the case. In fact, the integrated intensity values do not differ significantly from the theoretical point values plotted in Figures 15 and 17 through 27. Neither a correlation nor an explanation has been found which explains this disagreement. In this light--assuming no oversight has been committed in obtaining these results--the IPSS tables for the large-angle technique should be replaced. However, the ability to generate new tables also provides the ability to make the IPSS more versatile since parameters such as refractive index and angle pair can now be varied.

REFERENCES

1. van de Hulst, H. C., Light Scattering by Small Particles, Dover Publications, Inc., New York, 1981.
2. Hottel, H. C., A. F. Sarofim, I. A. Vasalos, and W. H. Dalzell, "Multiple Scatter: Comparison of Theory with Experiment," Journal of Heat Transfer, vol. 92, no. 2, pp 285-291, 1970.
3. Kerker, M., The Scattering of Light and Other Electromagnetic Radiation, Academic Press, New York, 1969.
4. Bohren, C. F. and D. R. Huffman, Absorption and Scattering of Light by Small Particles, John Wiley and Sons, New York, 1983.
5. Siegel, R. and J. R. Howell, Thermal Radiation Heat Transfer, McGraw-Hill Book Co., New York, 1981.
6. Dave, J. V., Subroutines for Computing the Parameters of the Electromagnetic Radiation Scattered by a Sphere, IBM 320-3237, IBM Corp., Palo Alto, Calif., May 1968.
7. Wiscombe, W. J., Mie Scattering Calculations: Advances in Technique and Fast, Vector-Speed Computer Codes, NCAR TN-140+STR, NCAR, Boulder, Colorado, June 1979.
8. Hirlemann, Jr., E. D., "Optical Technique for Particulate Characterization in Combustion Environments: The Multiple Ratio Single Particle Counter," Ph.D. Thesis, Purdue University, 1977.
9. Bohren, C. F. and A. J. Hunt, "Scattering of Electromagnetic Waves by a Charged Sphere," Canadian Journal of Physics, vol. 55, 1977.

APPENDIX A

MAXWELL'S EQUATIONS

The basic laws of electromagnetic radiation are known as Maxwell's equations and are listed below:

$$\nabla \cdot \vec{D} = \rho \quad \text{Gauss's Law for Electric Fields} \quad (\text{A-1})$$

$$\nabla \cdot \vec{B} = 0 \quad \text{Gauss's Law for Magnetic Fields} \quad (\text{A-2})$$

$$\nabla \times \vec{E} = - \frac{\partial \vec{B}}{\partial t} \quad \text{Faraday's Law} \quad (\text{A-3})$$

$$\nabla \times \vec{H} = \vec{J} + \frac{\partial \vec{D}}{\partial t} \quad \text{Ampere's Law} \quad (\text{A-4})$$

where \vec{D} = electric flux density or displacement flux density [C/m^2],

\vec{E} = electric field intensity [volts/m],

\vec{B} = magnetic flux density [Webers/ m^2],

\vec{H} = magnetic field intensity [A/m],

ρ = charge density [C/m^3],

\vec{J} = conduction and convection current density [A/m^2].

These terms are also related by the following:

$$\vec{D} = \epsilon \vec{E} \quad (\text{A-5})$$

$$\vec{B} = \mu \vec{H} \quad (\text{A-6})$$

$$\vec{J} = \sigma \vec{E} \quad (\text{A-7})$$

where ϵ = electric permittivity [farad/m],

μ = magnetic permeability [Henry/m],

σ = conductivity [mhos/m].

Although the point form of Equations (A-1) to (A-4) may appear confusing and meaningless to those who have not studied electromagnetic field theory, a physical representation can be drawn from the integral form of the equations.

A. GAUSS'S LAW FOR ELECTRIC FIELDS

By integrating $\nabla \cdot \vec{D} = \rho$ over any volume,

$$\int_V (\nabla \cdot \vec{D}) dV = \int_V \rho dV = Q$$

where q = total free charge in the volume, and applying the divergence theorem,

$$\int_V (\nabla \cdot \vec{F}) dV = \oint_S \vec{F} \cdot d\vec{S},$$

the integral form can be obtained

$$\oint_S \vec{D} \cdot d\vec{S} = Q.$$

This equation states that the amount of charge enclosed by a surface can be related to the lines of flux entering (for negative charges) or leaving (for positive charges) a surface (See Figure A-1).

B. GAUSS'S LAW FOR MAGNETIC FIELDS

In a similar manner, $\nabla \cdot \vec{B} = 0$, integrated over a volume becomes

$$\oint_S \vec{B} \cdot d\vec{S} = 0$$

This equation states that the net magnetic flux through a closed surface is always zero. In other words, the magnetic flux lines close upon themselves (See Figure A-2). The magnetic counterpart of an isolated electric charge--

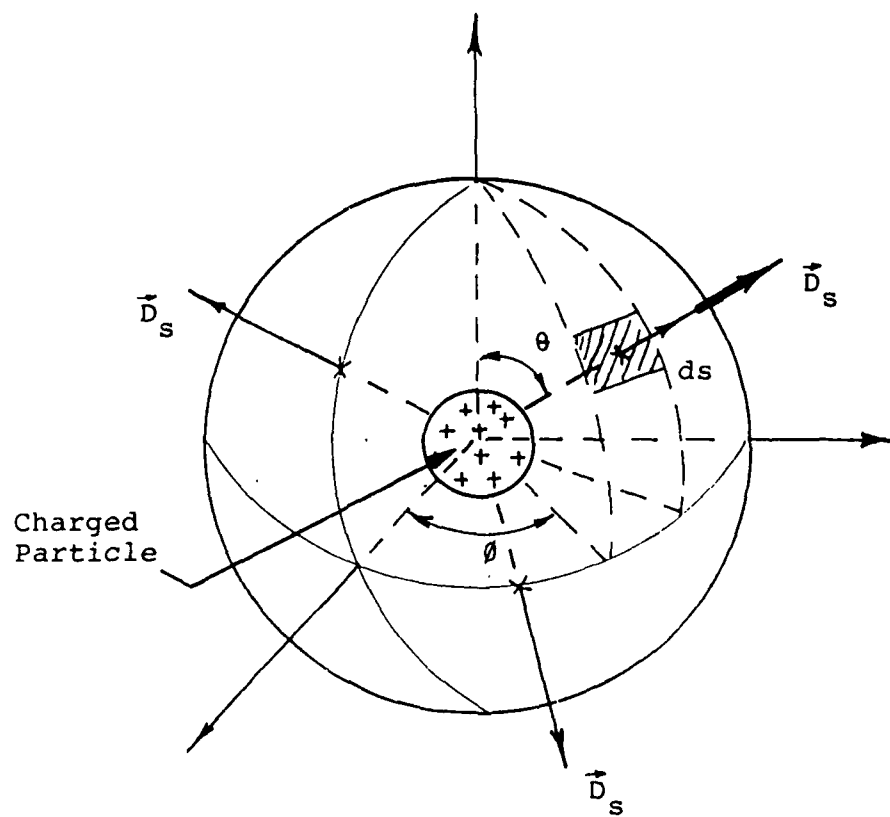


Figure A-1. A Physical Representation of Gauss's Law for Electric Fields

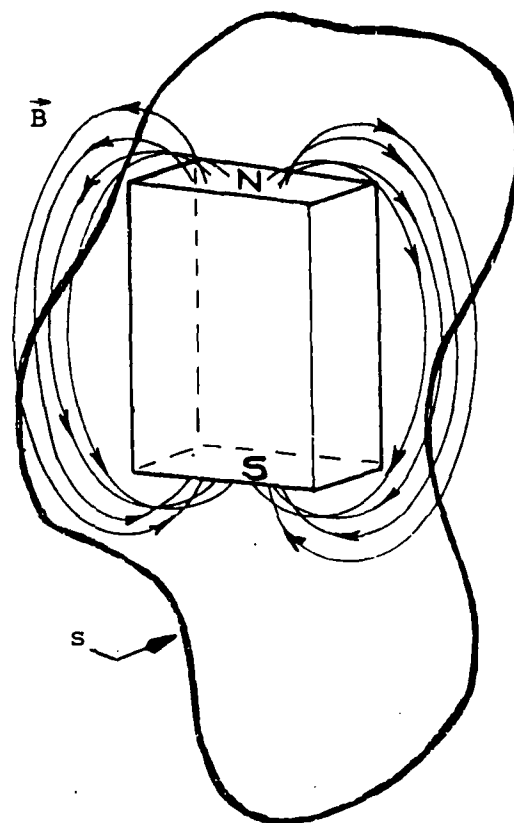


Figure A-2. A Physical Representation of Gauss's Law for Magnetic Fields

namely, a single magnetic pole--does not exist. For every north pole, a south pole exists.

C. FARADAY'S LAW OF INDUCTANCE

If the point form of Faraday's Law is integrated over a surface,

$$\int_S (\nabla \times \vec{E}) \cdot d\vec{S} = - \int_S \frac{\partial \vec{B}}{\partial t} \cdot d\vec{S}$$

Stokes Theorem can be applied to the left hand side to obtain

$$\int \vec{E} \cdot d\vec{l} = - \int \frac{\partial \vec{B}}{\partial t} \cdot d\vec{S}.$$

It can be seen that a time varying magnetic field ($\vec{H} \propto \vec{B}$) induces an electromotive force

$$\text{emf} = \oint \vec{E} \cdot d\vec{l}$$

which establishes a current in a closed circuit. An example of such a case is shown in Figure A-3. Here the movement of the magnet toward the closed circuit causes an increase in the magnetic flux through any arbitrary surface, S , enclosed by the coil, and as a result, the potential drop across the resistor increases in such a way as to oppose the increasing magnetic field. Note that although the previous example employed a physical closed conducting path, the path could be an imaginary line in space.

D. AMPERE'S LAW

The integral form of Ampere's Law can be written by again employing Stokes' Theorem to obtain

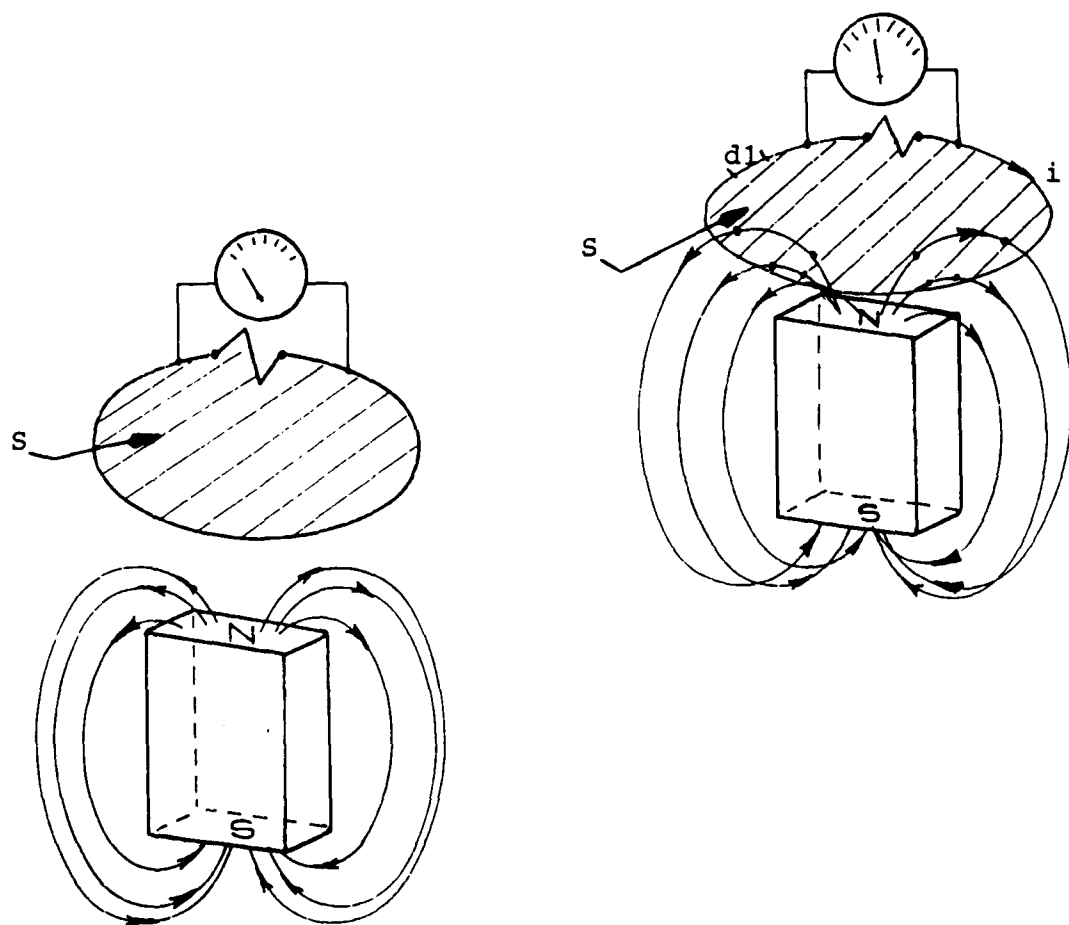


Figure A-3. A Physical Representation of Faraday's Law of Inductance

$$\oint \vec{H} \cdot d\vec{l} = \int_S \vec{J} \cdot d\vec{S} + \int \frac{\partial \vec{D}}{\partial t} \cdot d\vec{S}.$$

By dimensional analysis, it can be seen that the right hand side of the above equation are current terms where the first term is the conduction or convection current, and the second term is the displacement current. For example, consider the circuit shown below in Figure A-4. If a time-varying magnetic field pierces the plane, S, of the circuit, by Faraday's Law, an electric potential is induced in the conductor causing current to flow. The integration of the magnetic field tangential to the path, $d\vec{l}$, yields the current exiting the arbitrary surface enclosed by the path. At (a) the current leaving the surface is the conduction current

$$I_c = \int \vec{J} \cdot d\vec{S}$$

and the displacement current,

$$I_d = \int_S \frac{\partial \vec{D}}{\partial t} \cdot d\vec{S}$$

is zero. If the surface is made to cut between the plates of the capacitor at (b), $I_c = 0$ because charge is not being transmitted from one plate to another. However, the line integral still follows the same path; therefore, the total current calculated by each method must be equal. Thus, a displacement current exists between the plates of the capacitor causing the circuit to be complete.

E. BOUNDARY CONDITIONS

The previous equations will give expressions of the electromagnetic field as it propagates through a medium. However, if another medium is encountered, boundary conditions must be known at the interface.

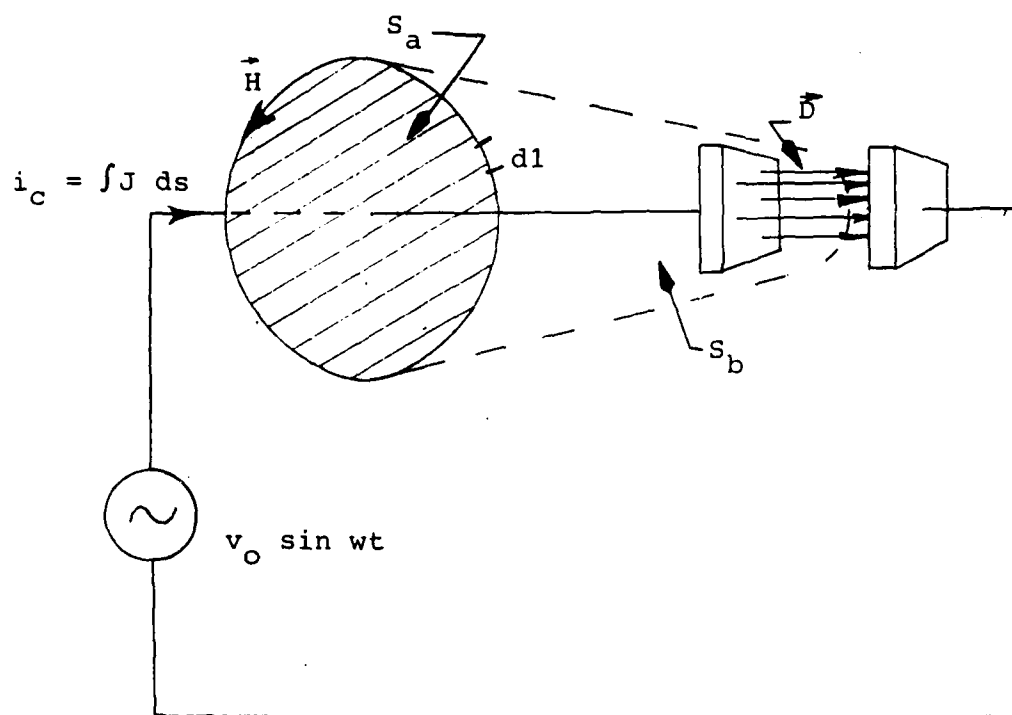


Figure A-4. A Physical Representation of Ampere's Law

From the integral form of Faraday's Law and Ampere's Law respectively, it can be shown that the electric field and magnetic field components tangential to the surface of the interface are continuous provided that \vec{J} , $\frac{\partial \vec{D}}{\partial t}$, and $\frac{\partial \vec{B}}{\partial t}$ remain finite as the surface area approaches zero. Thus,

$$E_{t,1} = E_{t,2}$$

(A-8a,b)

$$H_{t,1} = H_{t,2}$$

From Gauss's Law, the normal components of the electric flux density, and therefore, the electric field, are in general discontinuous across the boundary. Thus,

$$D_{n,1} - D_{n,2} = \rho_s$$

(A-8c)

$$\text{or } \epsilon_1 E_{n,1} - \epsilon_2 E_{n,2} = \rho_s,$$

where ρ_s is the free surface charge density existing on the boundary. Applying the same law to the normal magnetic field components, it is seen that

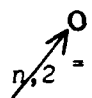
$$B_{n,1} = B_{n,2}$$

(A-8d)

$$\text{or } \mu_1 H_{n,1} = \mu_2 H_{n,2}$$

If the nature of the medium (i.e., conductor or insulator) is known, the boundary conditions can be made more specific. Consider first the case of the perfect conductor. Because no electromagnetic fields exist in the interior of

a perfect conductor (Figure A-5), the boundary conditions become

$$D_{n,1} - D_{n,2} = \rho_s$$


$$E_{t,1} = 0,$$

(A-9a,b,c,d)

$$B_{n,1} = 0,$$

$$H_{t,1} = K,$$

where K is the current per unit width flowing on the surface of the conductor perpendicular to the tangential magnetic field at the boundary of the surface. Note for a perfect conductor, that although the current flowing on the surface is finite, the current density \vec{J} is infinite. Therefore, Equation (A-8b) is no longer valid.

For a perfect insulator (dielectric), no free surface charge is present on the surface unless the charge was specifically placed there. In the case of no free surface charge, the boundary conditions become

$$D_{n,1} = D_{n,2}$$

$$E_{t,1} = E_{t,2}$$

(A-10a,b,c,d)

$$H_{t,1} = H_{t,2}$$

$$B_{n,1} = B_{n,2}$$

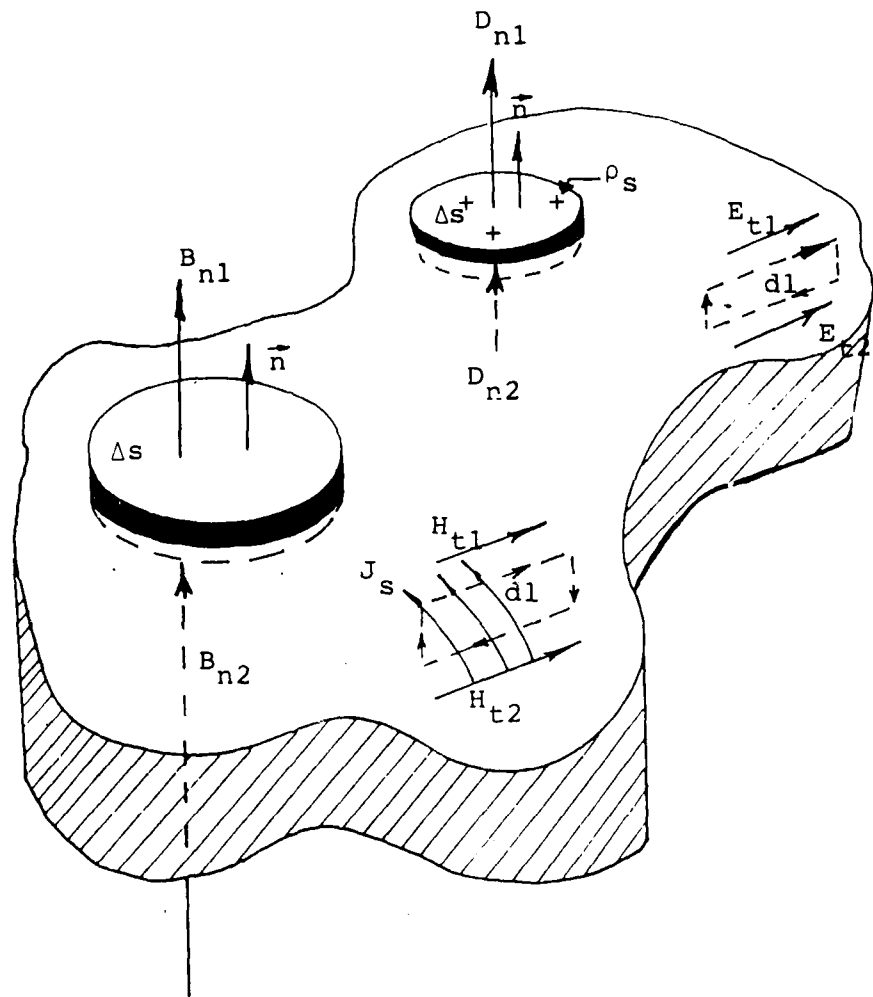


Figure A-5. A Representation of Boundary Conditions Between Two Different Media